Received: 13 February 2024 | Revised: 25 August 2024 | Accepted: 28 August 2024

DOI: 10.1002/joc.8614

RESEARCH ARTICLE

International Journal of Climatology RMetS

Synergistic interactions between urban heat islands and heat waves in the Greater Kuala Lumpur and surrounding areas

Sharifah Faridah Syed Mahbar[1,2] | **Hiroyuki Kusaka**[3]

[1]Graduate School of Life and Environmental Sciences, University of Tsukuba, Tsukuba, Japan

[2]Malaysian Meteorological Department, Petaling Jaya, Malaysia

[3]Center for Computational Sciences, University of Tsukuba, Tsukuba, Japan

Correspondence
Hiroyuki Kusaka, Center for Computational Sciences, University of Tsukuba, Tsukuba, Ibaraki 305-8577, Japan.
Email: kusaka@ccs.tsukuba.ac.jp

Funding information
JSPS KAKENHI, Grant/Award Number: JP24K07130; Multidisciplinary Cooperative Research Program in Center for Computational Sciences, University of Tsukuba

Abstract

The synergistic interactions between urban heat islands (UHI) and heat waves (HW) continue to be debated. Despite the expectations of UHI intensification during HW, several studies have demonstrated variations. Notably, there is a dearth of investigations concerning the UHI–HW synergy in tropical climate cities amidst the escalating trend of more frequent and severe HW in Southeast Asia. To address this gap, our study aimed to investigate the synergies between the UHI and HW phenomena in Greater Kuala Lumpur (GKL) and its surrounding areas. We employed the advanced research version 4.2.2 of the Weather Research and Forecasting (WRF) model, coupled with a single-layer Urban Canopy Model (UCM), to examine the impact of UHI during two heat wave events in 2016 (Case 1) and 2020 (Case 2), against the periods immediately before and after these events, which we refer to as Pre-Post HW (PPHW), in GKL. An elevated UHI intensity (UHII) was evident during the HW in both observations and simulations, with a noticeable distinction particularly observed in Case 1. During HW, observed data indicates average UHII peaks at 1.8°C (0100 LST (UTC+8)) and 1.7°C (1500 LST) in Cases 1 and 2, respectively. In contrast, those for PPHW days for Cases 1 and 2 are 1.5°C (0000 LST) and 1.2°C (0100 LST), respectively. The maximum observed heat loads are likely to occur at noon, reaching 2.3°C at 1600 LST in Case 1 and 3.7°C at 1500 LST in Case 2. LST stands for local standard time. Heat flux component analysis from the surface energy balance model confirmed the UHI–HW synergy. A notable difference in the Bowen Ratio between urban and rural areas highlights the effect of urbanisation on heat fluxes, potentially exacerbating urban discomfort during HW. Consistent across all measurement methods, the evidence indicates a clear and positive synergy between the UHI and HW in the GKL. This study can potentially deliver valuable insights, especially in urban planning, where the implications of weather events are substantial.

KEYWORDS

heat wave, Kuala Lumpur, synergy, tropical urban, urban heat island

1 | INTRODUCTION

The Earth's climate is undergoing profound changes, with urban environments at the forefront of the ramifications of a warming planet. The phenomenon of urban heat islands (UHI), characterised by elevated temperatures within urban areas compared to their surrounding rural landscapes, is a well-documented consequence of urbanisation (Oke, 1973). Urban warming adversely affects human health and reduces the thermal comfort of urban dwellers (Arifwidodo & Chandrasiri, 2020; Kusaka et al., 2012a; Klysik & Fortuniak, 1999; Imran et al., 2021; Morris et al., 2016a; Shaharuddin et al., 2014; Stafoggia et al., 2008; Vitanova & Kusaka, 2018; Vitanova et al., 2021).

Elsayed (2012) detailed past studies on UHI in Kuala Lumpur, where the pioneering work in this field can be attributed to Sham Sani, who delved into the subject in his initial paper published in 1972, focusing on aspects of the urban microclimate of Kuala Lumpur (Sham, 1972). He consistently studied the UHI until the early 90s, and among the prominent findings was that the UHI intensity (UHII) was higher during the night-time with calm and clear skies than during the daytime (Sham, 1990). A recent UHI study for Greater Kuala Lumpur (GKL), using the numerical modelling approach by Ooi et al. (2017), reported that daily mean UHII reached 0.9°C and was more severe at night-time at 1.9°C. A similar anomaly was observed more than 30 years after Sham Sani. The empirical investigation on UHI conducted by Ramakreshnan et al. (2018) found that the maximum UHII during dry, southwest monsoon (in June) is approximately 1.7°C for urban stations, compared to 1.3°C for suburban areas. In contrast, the findings by Shaharuddin et al. (2014) concluded that daytime UHII in the GKL is higher than night-time for all monsoon periods (Northeast: November–March, Southwest: June–August, and both intermonsoon: April–May and September–October). This diverse range of findings underscores the need for further exploration to gain a comprehensive understanding of this phenomenon.

Recently, extreme weather events, particularly heat waves, have occurred with increasing frequency and intensity (Li, 2020; Russo et al., 2014; Russo et al., 2015). Heat waves (HW) have long been recognised as the deadliest weather-related hazards and are responsible for some of the fatal natural disasters on record (Puley et al., 2022). Among the most popular references to deadly events is the 2003 European HW episode, which claimed more than 70,000 victims (Robine et al., 2007; Russo et al., 2014). In 2010, the European region was struck by another carcinogenic event known as the Russian HW, which was the worst event since 1950 (Russo et al., 2015). The Southeast Asia (SEA) region is no stranger to these extreme events, as evidenced by the April 2016 HW, which profoundly affected countries such as Malaysia and neighbouring Singapore. This event led to adverse outcomes, including decreased food production and subsequently elevated vegetable prices (Chew et al., 2020; Mohd Rasfan, 2016). Moreover, it induced drought conditions, leading to water rationing, especially in Kuala Lumpur and Selangor, and also triggered haze (Ahmad Kamal et al., 2019; Mohd Rasfan, 2016). In the realm of electricity infrastructure and consumption, 2016 saw an increase of 8.5% in installation capacity and 8.9% in consumption compared with 2015, and the peak electricity demand was recorded at 17,788 MW in April 2016 (Department of Statistics Malaysia, 2018). Additionally, Malaysia has reported a notable increase in heat-related illnesses and fatalities (Hamray & Choi, 2022; The Star/Asia News Network, 2016).

The coexistence of UHI and HW in urban settings poses a complex and interconnected challenge that warrants an in-depth exploration. In general, three distinct types of interactions can be identified. These interactions pertain to whether the intensity of the UHI increases (positive) (Ao et al., 2019; Hamray & Choi, 2022; Jiang et al., 2019; Li & Bou-Zeid, 2013; Ngarambe et al., 2020; Ramamurthy & Bou-Zeid, 2016; Tewari et al., 2019), decreases (negative) (Kumar & Mishra, 2019; Scott et al., 2018) or remains unchanged (neutral) (Chew et al., 2020; Ramamurthy & Bou-Zeid, 2016) during a HW. Notably, there is a significant research gap within tropical regions, especially among countries in SEA (Chew et al., 2020; Li, 2020) pertaining to this topic. This gap in research needs to be addressed to establish a firm understanding of this synergy, particularly in tropical cities that are at risk of more exposure to HW than cities in the mid-latitudes (Chew et al., 2020). Specifically, most SEA countries are projected to experience HW more frequently, with longer durations and increased intensity (Dong et al., 2021; Li et al., 2020). Addressing these two climate-related phenomena, UHI and HW is essential for advancing sustainable urban development and ensuring the well-being of residents in light of escalating climate challenges.

In a parallel context, Hamray and Choi (2022) conducted a study investigating the impact of HW on urban warming in Kuala Lumpur utilising the Community Land Model (CLM). However, the CLM cannot accurately consider land–atmosphere interactions. Numerical Weather Prediction (NWP) models, such as Weather Research and Forecasting (WRF), are necessary to thoroughly analyse these interactions. Furthermore, the WRF model, coupled with the urban canopy model (WRF-UCM), offers a robust framework for investigating UHI (Kusaka et al., 2001, 2012b; Kusaka & Kimura, 2004).

In this study, we aim to unravel the synergies between the UHI and HW phenomena in GKL and its adjacent areas by delving into the following key inquiries:

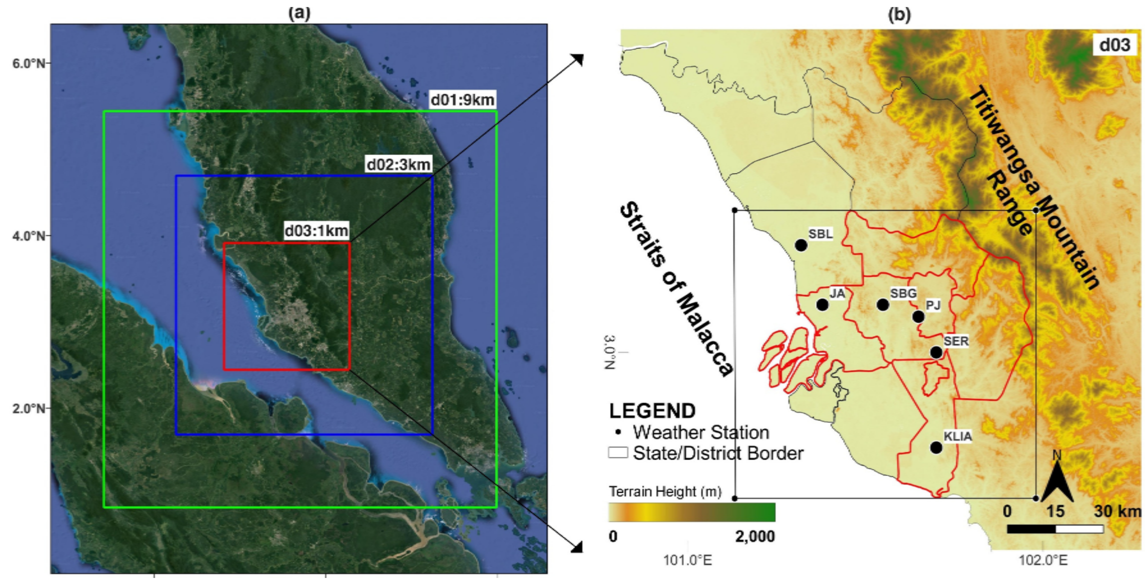

FIGURE 1 Study area. (a) Domain design and setup. The outer boundary (green) covers the parent domain (d01), while d02 (blue) and d03 (red) represent the second and third domains, respectively. (b) The terrain height of the target area. Fuzzy red lines and black lines mark the GKL area and the districts' administrative borders, respectively. The black dots indicate the locations of weather stations that supply data for verification and analysis. The black square is the area within d03 where spatially averaged computation for urban and rural categories is conducted. [Colour figure can be viewed at wileyonlinelibrary.com]

- How does urbanisation affect the intensity of UHI in GKL?
- What disparities exist in the observed UHII between HW and the Pre-Post HW (PPHW) days in GKL?
- What variations are observed in the surface heat budget during HW days compared with PPHW days?

In this study, we define "synergy" as the interactive effects of the UHI and HW that intensify the overall impact beyond the influence of either phenomenon alone (e.g., Ao et al., 2019; Li & Bou-Zeid, 2013; Ngarambe et al., 2020). This synergistic interaction is crucial for understanding the combined effects of urbanisation and extreme heat events on local and regional climates.

The remainder of this paper is structured as follows: section 2 presents the data and methodology, section 3 presents the results, section 4 involves the discussion and section 5 provides the conclusions and remarks.

2 | DATA AND METHODOLOGY

2.1 | Study area: GKL, Malaysia

GKL, Malaysia's most highly urbanised conurbation (Ooi et al., 2017), encompasses ten local governments. These include the metropolitan city of Kuala Lumpur, the administrative capital of Putrajaya, and the eight surrounding local authority regions: Petaling Jaya, Subang Jaya, Shah Alam, Ampang Jaya, Selayang, Kajang, Klang and Sepang. Together, they form an urban agglomeration spanning 2793 km^2 (Yasin et al., 2022). Kuala Lumpur City, in particular, boasts a notably high population density, reaching its peak of 7188 people per square kilometre (Husin et al., 2021). Situated on the west coast of Peninsular Malaysia, the GKL is bordered by the Strait of Malacca to the west and the Titiwangsa Mountain Range to the east, as illustrated in Figure 1. Like Peninsular Malaysia, it features a tropical rainforest climate with a specific designation type, Af, in the Köppen–Geiger climate classification, characterized by an average annual temperature of 25.8°C and a precipitation of 2500 mm (Hamray & Choi, 2022). February/March is recognised as the hottest period in Kuala Lumpur, with monthly peak temperatures ranging between 32 and 33°C, while December marks the coolest month, with the highest temperature of 31°C (Elsayed, 2012). Weather patterns in Peninsular Malaysia are significantly influenced by two primary factors: the Asian-Australian monsoon and prevailing winds (Jamaluddin et al., 2018; Tangang et al., 2017). From June to August, the region experiences southwesterly winds, whereas from December to February, northeasterly winds dominate, locally known as the southwest and northeast monsoons, respectively. Additionally, the region experiences an intermonsoon period from March to April and September to November.

TABLE 1 Model configurations.

Model version: WRF4.2.2-ARW			
Runtime	Case 1: March 26, 0800 LST–April 8, 0800 LST, 2016 Case 2: April 15, 0800 LST–April 24, 0800 LST, 2020		
Research period	Case 1: March 28, 0000 LST–April 8, 0000 LST, 2016 Case 2: April 17, 0000 LST–April 24, 0000 LST, 2020		
Parent data	NCEP GDAS/FNL (6-hourly data; 0.25° spatial resolution)		
SST data	OISST ver. 2.1 (daily; 0.25° horizontal resolution)		
Domain	d01	d02	d03
Grid spacing (km)	9	3	1
Grid cell numbers	50 × 50	97 × 97	142 × 142
No. of vertical layers	33 layers		
Land surface model	Noah-MP Land Surface Model (Niu et al., 2011; Yang et al., 2011)		
Urban canopy model	Single-layer UCM (Chen et al., 2011; Kusaka et al., 2001; Kusaka & Kimura, 2004)		
Microphysics	Thompson Scheme (Thompson et al., 2008)		
Planetary boundary layer (PBL)	Yonsei University Scheme (Hong et al., 2006)		
Shortwave radiation	Dudhia Shortwave Scheme (Dudhia, 1989)		
Longwave radiation	RRTM Longwave Scheme (Mlawer et al., 1997)		
Cumulus	New Tiedtke Scheme (Zhang & Wang, 2017)	x	x

2.2 | Model configuration and settings

The WRF-ARW model (version 4.2.2) coupled with a single-layer Urban Canopy Model (WRF-UCM) was used in this study. The physical options are listed in Table 1. The urban surface parameters described by Morris et al. (2016b) were adopted while examining urbanisation in GKL. Their previous work on the urbanisation and urban climate of Klang Valley, Malaysia (also known as GKL) successfully simulated a 2 m surface temperature (T2), 2 m relative humidity (RH) and 10 m wind. Therefore, this setting was deemed reliable for use in the present study. Three-nested model domains were designed with spatial grid resolutions of 9, 3 and 1 km (see Figure 1). All domains were centred at 3.15°N and 101.7°E, with Kuala Lumpur as the main reference. The Mercator projection was used in this study because it is suitable for low-latitude domains (Wang et al., 2019). The setting of the nesting boundary is also considered the best practice for avoiding the border from being set over higher terrain or mountainous areas while reducing simulation bias.

NCEP GDAS/FNL 0.25 Degree Global Tropospheric Analysis and Forecast Grids (FNL) with a temporal resolution of 6 h were used to create a lateral boundary condition (LBC). Isa et al. (2020) concluded that the higher temporal and spatial resolution of LBC, for instance, the FNL, can regenerate the tropical urban climate conditions of Kuala Lumpur and reliably portray the near-surface temperature of tropical cities. The NOAA Daily Optimum Interpolation Sea Surface Temperature (OISST) version 2.1 was employed in this study (Huang et al., 2021). The data were updated at daily intervals in the WRF. Both simulations involved a spin-up period of 40 h, with Case 1 starting on March 26, 2016 at 0800 LST (UTC+8) and Case 2 on April 15, 2020 at 0800 LST. The research period for Case 1 spanned 11 days, from March 28, 2016 at 0000 LST to April 8, 2016 at 0000 LST, while Case 2, lasted for 7 days, from April 17, 2020 at 0000 LST to April 24, 2020 at 0000 LST. LST is local standard time.

2.3 | Land use/land cover map

We depicted the influence of urbanisation on UHI in the GKL using the Moderate Resolution Imaging Spectroradiometer (MODIS) land use and land cover (LULC) data. The default MODIS dataset in WRF, known as MODIS-15s, which corresponds to a grid spacing of approximately 450 m, was used as the input LU data in this study. Each grid point represents the surface type of LULC according to the MODIS classification. MODIS land cover datasets are among the most prominent datasets extensively employed as inputs for static data in urban climate studies and have consistently demonstrated their ability to produce reliable impacts on results (Golzio et al., 2021). Initially designated for urban and built-up areas, the MODIS datasets were refined by adjusting for the urban category. This adaptation allowed compatibility with the WRF-UCM model and resulted in classification under the urban categories of 31 (low-intensity residential), 32 (medium-intensity residential) and 33 (high-intensity residential/commercial/industrial). In contrast, rural grid points encompass diverse natural land cover types, including forests, shrublands, vegetation and croplands. Information on the data availability and details of the weather stations that supply data

TABLE 2 Observation data information.

Weather station				Classification LULC	Modification LULC		HW analysis
					WRF-UCM		
Name	ID	Lat (N)	Lon (E)	MODIS-15s	URB	non-URB	Period
Petaling Jaya	PJ	3.10	101.65	Urban and build up—commercial	High intensity residential/ industrial/commercial	Cropland/natural vegetation	1981–2010
Serdang	SER	3.00	101.70				-
Subang	SBG	3.13	101.55				1981–2010
Klia	KLIA	2.73	101.70				-
Jalan Akob	JA	3.13	101.38	E. broadleaf forest	-	-	-
Sg Buloh	SBL	3.30	101.32	E. broadleaf forest	-	-	-

for model verification, LULC modification and HW analysis are provided in Table 2.

2.4 | Anthropogenic heat emission datasets

Anthropogenic heat emission (AHE) is produced within urban areas and plays a pivotal role in subsidising the UHI (Klysik & Fortuniak, 1999; Kondo & Kikegawa, 2003; Sailor, 2010; Vitanova & Kusaka, 2018). Present-day AHE datasets (the 2010s) in unit W·m^{-2}, known as AH4GUC by Varquez et al. (2021), were used in this study. The spatial resolution was approximately 1 km, and the datasets encompassed spatial changes resulting from urban sprawl anomalies and climate change scenarios. The construction of AH4GUC also employs a "top-down" approach, typically involving the derivation of energy consumption data from regional or national levels, which is subsequently downscaled to generate gridded information.

Our group modified the WRF-UCM model used in this study to provide a two-dimensional distribution of the AHE. This modification allowed us to spatially distribute AHE according to the urban land use categories within our model domain. This method, which is particularly effective for urban-dominant grids, allows for a more accurate representation of heat fluxes associated with urbanisation, as demonstrated in recent work by Magnaye and Kusaka (2024). To ensure that the modified AHE data was accurately reflected in the simulation, we ran "geogrid.exe" as part of the WRF preprocessing system (WPS). This step generated the necessary geographical data, including the updated AHE distribution, which was then used by the UCM to simulate the impact of anthropogenic heat on the urban energy balance and urban temperatures. The AHE dataset is available monthly and temporally. Figure 2 displays the LULC information along with the spatiotemporal distribution of the AHE employed in this study. The fluxes ranged from approximately 5–80 W·m^{-2} within urban areas around 1600 LST in April. Figure 3 illustrates the diurnal variation in the AHE in the GKL.

2.5 | Statistical method and analysis: HW selection/identification

This study identified HW days by referring to the Heat Wave Magnitude Index daily (HWMId) developed by Russo et al. (2015). Here, HWMId is defined as the maximum magnitude of HW in a year, considering its intensity and duration.

The HWMId function incorporated within the hwmiextRemes package version 2.1-3 (Russo et al., 2014, 2015) served as the basis for selecting and identifying the study period. This study used temperature datasets from two urban stations, PJ and SBG (see Table 2), with data spanning over 30 years (1981–2010) and calculated the HWMId. The computation of the index depends on the daily maximum temperature value (Tmax) surpassing the 90th percentile threshold for a minimum duration of three consecutive days. The reference threshold was established over a baseline period of 30 years centred within a 31-day window. The interquartile range (IQR), which is the temperature difference between the 25th and 75th percentiles of Tmax, served as the unit for measuring HW magnitude. This choice is based on its non-parametric nature, which makes it a reliable measure of temperature variability. In this context, a HW day with a temperature equal to the IQR was assigned a magnitude of 1. By this definition, if the magnitude on a given day,

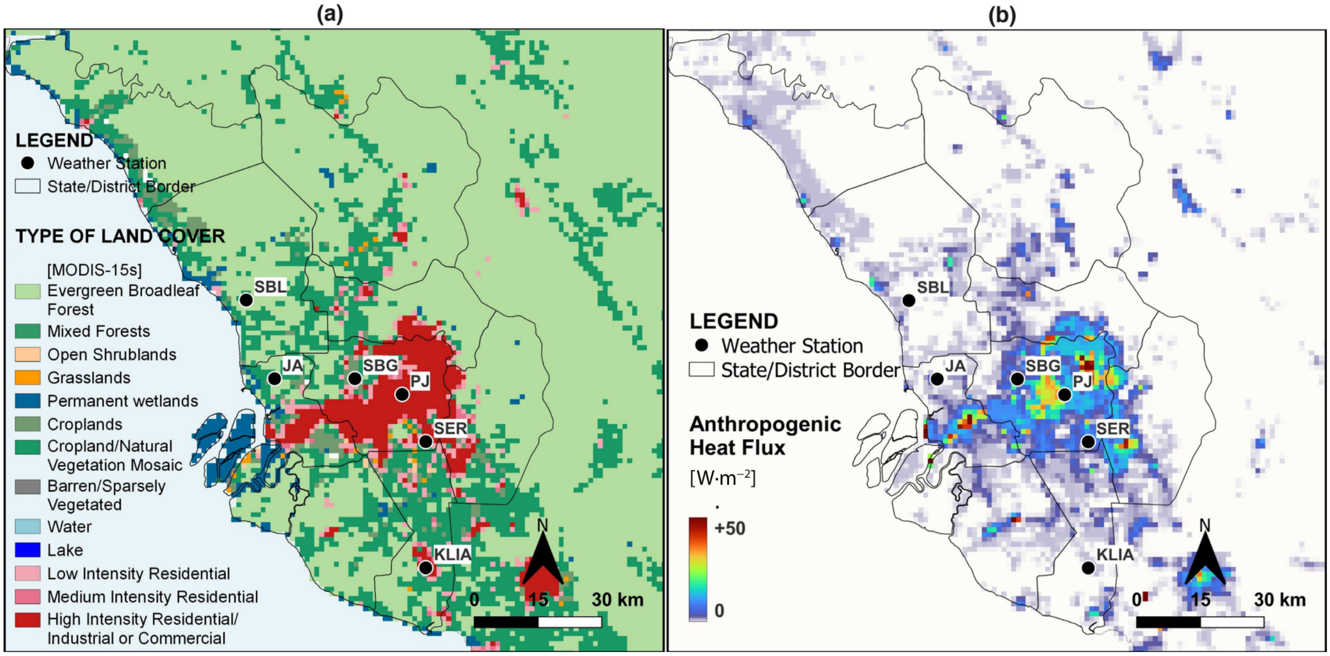

FIGURE 2 LULC map and spatiotemporal distribution AHE of d03 includes GKL areas. (a) MODIS dataset with a higher 15-arc-seconds resolution corresponding to grid spacing ∼450 m known as MODIS-15s. (b) Spatiotemporal distribution of hourly AHE for April at 0800 UTC (1600 LST). [Colour figure can be viewed at wileyonlinelibrary.com]

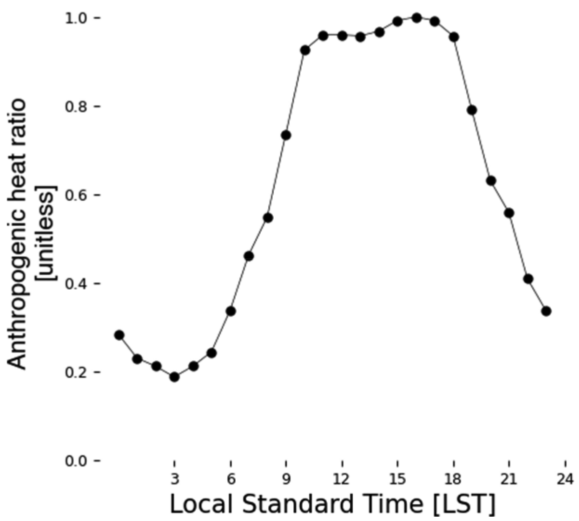

FIGURE 3 Diurnal profile of AHE in GKL. The observed peaks were around 1500–1700 LST with the maximum heat flux of 72.2 W·m^{-2} at central KL and 26.7 W·m^{-2} in residential areas.

denoted as "*d*" is 3, it signifies that the temperature anomaly on that day is three times the IQR.

Furthermore, change-point detection analysis using Pettitt's test has been used to identify abrupt changes or shifts in a time-series dataset (Jaiswal et al., 2015). In this study, the test helped pinpoint when significant changes in Tmax occurred. This finding supports the identification of HW cases using the HWMId.

2.6 | UHI analysis

To calculate UHI intensity, we employed two methods of UHII computation (Chew et al., 2020; Li et al., 2013). The first method involves direct calculations to obtain the UHII at specific locations (station-based) by considering the differences between urban and rural stations. The second method involved utilising the WRF-UCM by calculating the difference between the urban setting simulation (URB) and the "no urban" setting simulation (non-URB) to extract the impact of urbanisation. To obtain a non-URB setting, we modified the urban surfaces by assigning them the nearest grid vegetation type, corresponding to type 14 (Cropland/Natural Vegetation Mosaic) in this case. The computation of the UHII using URB and non-URB settings is also referenced in Chew et al. (2020) and Li et al. (2013) as an urban increment method.

In this study, Equation (1) was applied to compute the UHII (Chew et al., 2020; Doan et al., 2016; Doan & Kusaka, 2016; Vitanova & Kusaka, 2018) for the HW and PPHW periods. The term PPHW refers to the periods that immediately precede and follow HW events and are characterised by Tmax anomalies falling below the 90th percentile threshold. This definition assumes that these periods are the critical phases of adaptation and recovery in response to HW events. The HW and PPHW days for Cases 1 and 2 are presented in Table 3. Subsequently,

TABLE 3 Details of the HWMId output from Petaling Jaya (PJ) station.

		HW		PPHW	
Case	HWMId	Period	Duration (days)	Period	Duration (days)
1	9.8	March 29–April 4, 2016	7	March 28 to April 5–7, 2016	4
2	2.7	April 18–21, 2020	4	April 17, 22–23, 2020	3

Equation (2) was used to measure the difference in the UHII, referred to as the heat magnitude or heat load (HM), which represents the increase or decrease in the UHII during HW (Ward et al., 2016),

$$\text{UHII} = \overline{T}_{\text{URB}} - \overline{T}_{\text{non-URB}}, \tag{1}$$

$$\text{HM} = \text{UHII}_{\text{HW}} - \text{UHII}_{\text{PPHW}}. \tag{2}$$

3 | RESULTS

3.1 | Statistical method and analysis: Selecting/identifying HW cases

GKL experiences warmer temperatures between January and May compared to June and December (Figure S1, Supporting Information). Examining the 99th percentile of the daily Tmax distribution by month for the recent 10 years (2011–2020) at the urban stations made it evident that the distribution was overwhelmingly dominated by records from March to April (Figure S2). The extreme HW cases identified occurred in the same month. In Case 1, extreme HW occurred in 2016, spanning from March 29 to April 4. In Case 2, an extreme HW event was identified from April 18 to April 21, 2020.

The mean geopotential height at 500 hPa from the ECMWF Reanalysis V5 (ERA5) datasets at 0800 LST (Figure S3) indicates that persistent high-pressure ridging during the 2016 HW resulted in intense and prolonged heat, leading to a higher HW magnitude than that in 2020 (see Table 3). Interestingly, although the overall HW magnitude was lower in 2020, the heat index was higher. Specifically, the WBGT heat index (Dimiceli et al., 2012) revealed that the heat index reached 35.5°C (at 1600 LST on March 30) in Case 1 and 37.2°C (at 1400 LST on April 20) in Case 2. Both heat index values fall within the "hazardous" category, posing a risk of heat-related disorders for residents. This discrepancy arises because the HW index is based solely on the daily Tmax, whereas the heat index incorporates humidity as a critical variable. Under hot and humid conditions, the effectiveness of evaporative cooling diminishes,

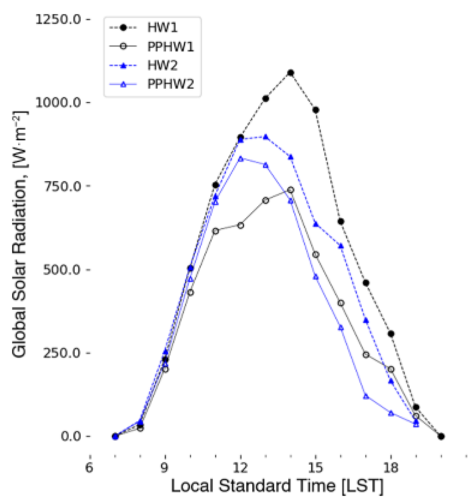

FIGURE 4 The diurnal distribution of global solar radiation at the observation station SBG during HW and PPHW days in Case 1 (black) and Case 2 (blue). The figure clearly indicates that solar radiation during HW days consistently exceeds that during PPHW days in both cases. [Colour figure can be viewed at wileyonlinelibrary.com]

potentially leading to increased core body temperature (Li et al., 2020). The interaction of these variables makes studying the UHI effects and HW in tropical cities uniquely challenging.

The prevailing winds at the 850 hPa level based on the ERA5 datasets at 0800 LST (see Figure S4) facilitate the transport of moist air from the Pacific Ocean to Peninsular Malaysia, including the GKL region, during the 2020 HW. This continued influx of moisture into the region contributes to higher humidity levels, leading to a higher heat index. In contrast, during the 2016 HW, low-pressure systems actively formed over the midlatitude region, dictating the movement of air masses and concentrating the wind flow in these areas. This resulted in a reduction in moisture influx from the Pacific Ocean to the region. Additionally, the 2016 HW coincided with an El Niño event, characterised by warmer-than-average sea surface temperatures (SST) in the central and eastern tropical Pacific, which disrupted normal atmospheric circulation and reduced cloud cover and rainfall in mainland SEA, including Peninsular Malaysia (Thirumalai et al., 2017). This reduction in cloud cover potentially

TABLE 4 Model simulation validation of 2 m temperature (°C), 2 m relative humidity (%) and 10 m wind speed for Case 1.

		T2				RH				Wind speed			
Case 1	ID	MBE	MAE	RMSE	*R*	MBE	MAE	RMSE	*R*	MBE	MAE	RMSE	*R*
HW	PJ	−0.10	0.97	1.27	0.92	−0.67	7.45	9.23	0.79	0.69	0.99	1.35	0.43
	SER	1.14	1.36	1.72	0.94	−0.63	5.62	6.88	0.90	0.74	0.93	1.12	0.50
	SBG	0.69	1.02	1.36	0.94	−4.54	8.01	10.59	0.81	0.05	0.70	0.89	0.68
	KLIA	1.05	1.13	1.35	0.96	5.13	8.13	9.77	0.81	1.30	1.95	2.36	0.13
	JA	0.28	0.87	1.07	0.96	−6.99	8.48	10.54	0.87	1.15	1.81	2.05	0.42
	SBL	−0.58	0.82	1.04	0.97	−16.30	16.31	17.59	0.91	2.06	2.11	2.47	0.10
PPHW	PJ	0.46	1.24	1.82	0.75	0.10	7.43	10.60	0.67	0.92	1.05	1.34	0.43
	SER	1.35	1.80	2.36	0.79	0.16	6.01	8.37	0.84	0.79	0.89	1.02	0.68
	SBG	1.03	1.43	2.21	0.73	−3.06	9.11	12.15	0.66	0.44	1.14	1.35	0.35
	KLIA	0.78	1.30	1.95	0.79	6.01	9.41	11.76	0.72	1.37	2.15	2.63	0.11
	JA	0.30	0.91	1.15	0.92	−0.58	7.74	10.08	0.75	1.83	1.90	2.15	0.23
	SBL	0.01	0.72	0.89	0.95	−10.81	11.56	14.22	0.82	1.90	1.93	2.26	0.22

increased the levels of solar radiation reaching the Earth's surface during the 2016 HW compared with the 2020 HW, as evidenced by data from the urban SBG station shown in Figure 4. The figure also highlights the noticeable discrepancy in solar radiation, with elevated levels observed during HW conditions compared to PPHW.

Diverging from the common practice in UHI–HW synergy studies, which primarily emphasises summer HW (known as the southwest monsoon period in Malaysia), this research emphasises the interaction between UHI and extreme HW events during the intermonsoon period in the GKL. These exceptional HW events have been statistically observed to occur mainly during March and April within the intermonsoon period, marking the transition from the wet to the dry season. During this transition period, the large-scale atmospheric pressure systems driving the monsoons are weaker and less dominant. This synoptic condition within the intermonsoon allows the specific physical characteristics of the local climate to take precedence (Li et al., 2013; Ooi et al., 2018a, 2018b).

3.2 | Model validation

The validation process of the model involved a comparison with data from six weather observation stations under the Malaysian Meteorological Department (MET Malaysia), which are strategically positioned across the GKL. The assessment of mean model biases entails the utilisation of three error indices, namely the mean bias error (MBE), mean absolute error (MAE) and root-mean-square error (RMSE), to gauge the statistical robustness between the model output and observed datasets.

3.2.1 | 2 m temperature, 2 m relative humidity and 10 m wind speed

Tables 4 and 5 present the model performance outcomes for Cases 1 and 2 on both HW and PPHW days. The urban stations are denoted as PJ, SER, SBG and KLIA, whereas the rural stations are represented by JA and SBL (see Table 2). Overall, the WRF-UCM simulation accurately reproduced the diurnal profiles of both T2 and RH in both cases. From the model bias analysis, the WRF-UCM excelled in predicting T2 for both cases, displaying smaller RMSE values (≤2.0°C) with a strong positive linear relationship. Specifically, during HW days, the biases for T2 are consistently smaller, with RMSE ranging from 1.0 to 1.7°C in Case 1 and 0.9 to 1.6°C in Case 2, compared to PPHW days where RMSE values ranged from 0.9 to 2.4°C in Case 1 and 1.7 to 2.3°C in Case 2. Similarly, this pattern holds for RH, with most of the stations showcasing RMSE values below the threshold of ≤10.0% with a strong positive linear relationship. It is noteworthy that this threshold validity aligns with that of Chew et al. (2020) and Ramamurthy and Bou-Zeid (2016).

A significant disparity in the diurnal T2 and RH profiles was observed during the transition from HW to PPHW days in both the observations and the WRF simulations, as depicted in Figure 5. The WRF effectively captures these diurnal profiles and distinguishes variations between urban and rural environments. During the HW

TABLE 5 Model simulation validation of 2 m temperature (°C), 2 m relative humidity (%) and 10 m wind speed for Case 2.

		T2				RH				Wind speed			
Case 2	ID	MBE	MAE	RMSE	*R*	MBE	MAE	RMSE	*R*	MBE	MAE	RMSE	*R*
HW	PJ	0.10	0.86	1.25	0.92	2.59	6.85	8.15	0.87	0.96	1.10	1.37	0.59
	SER	0.43	0.98	1.23	0.95	0.33	4.61	5.95	0.93	0.81	0.97	1.19	0.42
	SBG	0.08	1.17	1.57	0.89	−6.03	7.72	10.58	0.84	0.11	0.92	1.19	0.56
	KLIA	0.35	0.92	1.43	0.89	4.87	9.62	12.08	0.67	1.94	2.13	2.45	0.38
	JA	−0.34	0.70	0.89	0.97	3.11	8.56	9.52	0.93	1.21	1.29	1.56	0.35
	SBL	−0.27	0.96	1.28	0.93	−3.42	6.85	8.61	0.94	1.36	1.48	1.95	0.28
PPHW	PJ	0.79	1.36	2.00	0.80	−1.42	7.14	10.15	0.77	1.17	1.32	1.63	0.39
	SER	1.17	1.44	2.27	0.81	−5.08	6.34	9.54	0.85	0.86	0.99	1.29	0.34
	SBG	0.47	1.36	2.13	0.80	−6.63	8.47	11.41	0.81	0.54	1.03	1.30	0.42
	KLIA	1.20	1.41	2.39	0.75	−0.99	7.65	11.05	0.67	2.26	2.29	2.84	0.52
	JA	−0.14	1.25	1.72	0.88	5.20	8.66	10.14	0.92	1.35	1.43	1.99	0.30
	SBL	0.51	1.16	1.81	0.86	−3.68	6.04	8.40	0.90	1.19	1.41	1.89	0.16

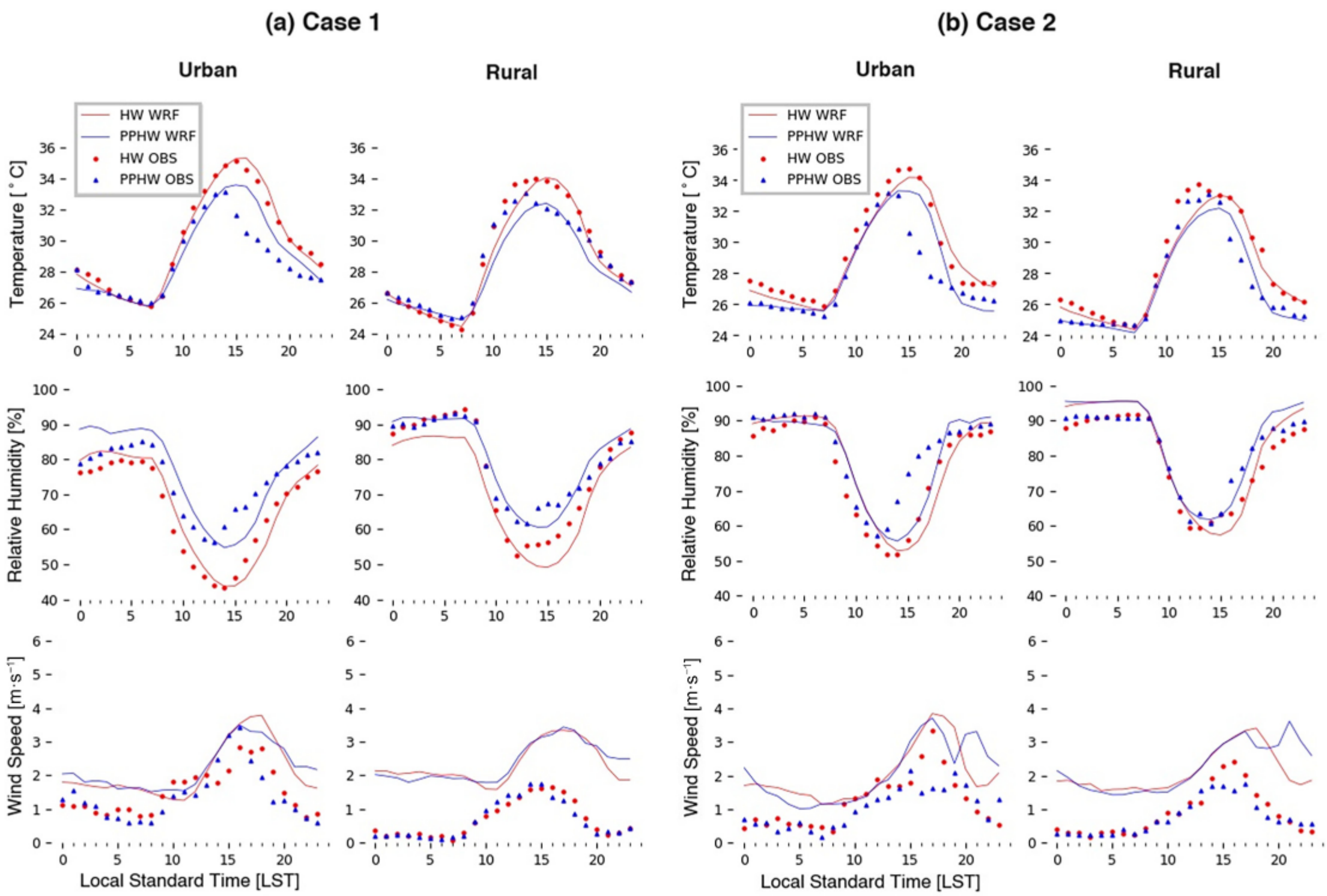

FIGURE 5 The diurnal profiles of 2m temperature (T2), 2m relative humidity (RH) and 10-m wind speed for both urban and rural categories during HW and PPHW days in Cases 1 and 2. Urban profiles are based on four urban stations (PJ, SER, SBG and KLIA), and rural profiles are based on two stations (JA and SBL). The circles represent the observation data, while solid lines depict the WRF simulation. Throughout HW, T2 and RH consistently surpasses that of PPHW days in both cases. A distinct profile in T2 and RH between urban and rural areas is clearly observable, particularly from midday until night-time. Wind speed variations are less pronounced in both scenarios. [Colour figure can be viewed at wileyonlinelibrary.com]

events, T2 was notably higher than during the PPHW. Specifically, the average daytime peak reached 35.2°C (Case 1) and 34.7°C (Case 2) in urban areas during HW events, compared to 33.2°C (Case 1) and 33.1°C (Case 2) during PPHW periods. This distinction highlights the substantial temperature increase associated with the HW conditions. Similarly, variations in RH were also observed, where a lower peak was observed between 1300 and 1600 LST during HW events, dropping to as low as 42% (Case 1) and 52% (Case 2) in urban areas and 50% (Case 1) and 58% (Case 2) in rural areas. This is compared to the RH levels of 55% (Case 1) and 58% (Case 2) in urban areas and 62% (both cases) in rural areas during the PPHW.

Additionally, the WRF model successfully reproduced night-time temperatures in all scenarios, beginning at midnight and continuing until sunrise. However, the model tends to delay forecasting the peak of T2 over rural areas by 1–2 h compared with the observed data. Theeuwes et al. (2015) discovered that the delay behaviour was due to the influence of atmospheric boundary layer conditions, leading to a higher morning heating rate in rural environments than in urban areas. The WRF consistently overpredicted T2 from 1400 to 2200 LST for Case 1 and from 1400 to 1800 LST for Case 2 in urban areas during PPHW days. The primary factor contributing to this overprediction appears to be the inability of the model to accurately simulate precipitation events during these specified timeframes, resulting in an overestimation of surface temperatures. Overall, both observations and simulations indicate that heat waves significantly elevate temperatures and reduce relative humidity. This highlights the model's greater robustness in simulating HW periods, where atmospheric interactions are less complex, compared to PPHW periods, which involve more intricate atmospheric processes such as precipitation events. Moreover, it is worth noting that a clear distinction between HW and PPHW days, characterised by a range of differences in T2 and RH profiles, was particularly evident during the Case 1 event.

We also validate the 10 m wind speed simulations, as wind circulation significantly influences the interaction between the UHI and HW (Ao et al., 2019). Although the WRF model tended to overestimate wind speeds at both the urban and rural stations (Tables 4 and 5), it effectively captured their diurnal patterns (Figure 5). Notably, both observations and simulations show ambiguous distinctions in wind speed variations during HW events, lacking the typical reductions reported in other studies (Ao et al., 2019; Li et al., 2016; Ngarambe et al., 2020) or increases (Li et al., 2016). It is worth highlighting that several factors could contribute to the larger RMSE value and overestimation of wind speed. For instance, the influence of surface roughness parameters, as discussed by Varquez et al. (2014), can significantly affect wind speed simulations. Additionally, the representation of urban morphological characteristics (Wang et al., 2020) is another important factor to consider.

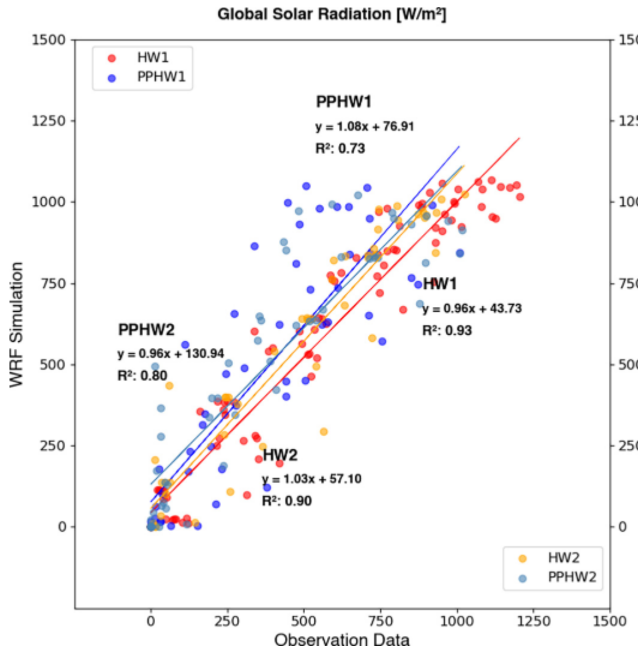

FIGURE 6 The correlation results of solar radiation between the urban station SBG and the WRF simulation for all scenarios. As the figure details, the linear relationship between the variables is expressed in the accompanying equation. The spatially average solar radiation of LULC type 33 (represents high intensity residential/commercial/industrial) derived from the simulation under the URB setting. [Colour figure can be viewed at wileyonlinelibrary.com]

In addition, while the observational datasets used are among the best available for validation, the limited number of representative observation sites may contribute to uncertainties and potential limitations in the results. This concern has been discussed in several studies (e.g., Tapiador et al., 2017), which highlight the impact of station density and representativeness on model validation and bias assessment can lead to inaccuracies or unsupported conclusions when evaluating model performance.

3.2.2 | Heat fluxes component: Global solar radiation

Global solar radiation data, or downward (incoming) shortwave radiation, are essential in climate modelling because they directly influence the surface energy balance and local climate conditions. In this study, we utilised the urban station SBG to validate the WRF model

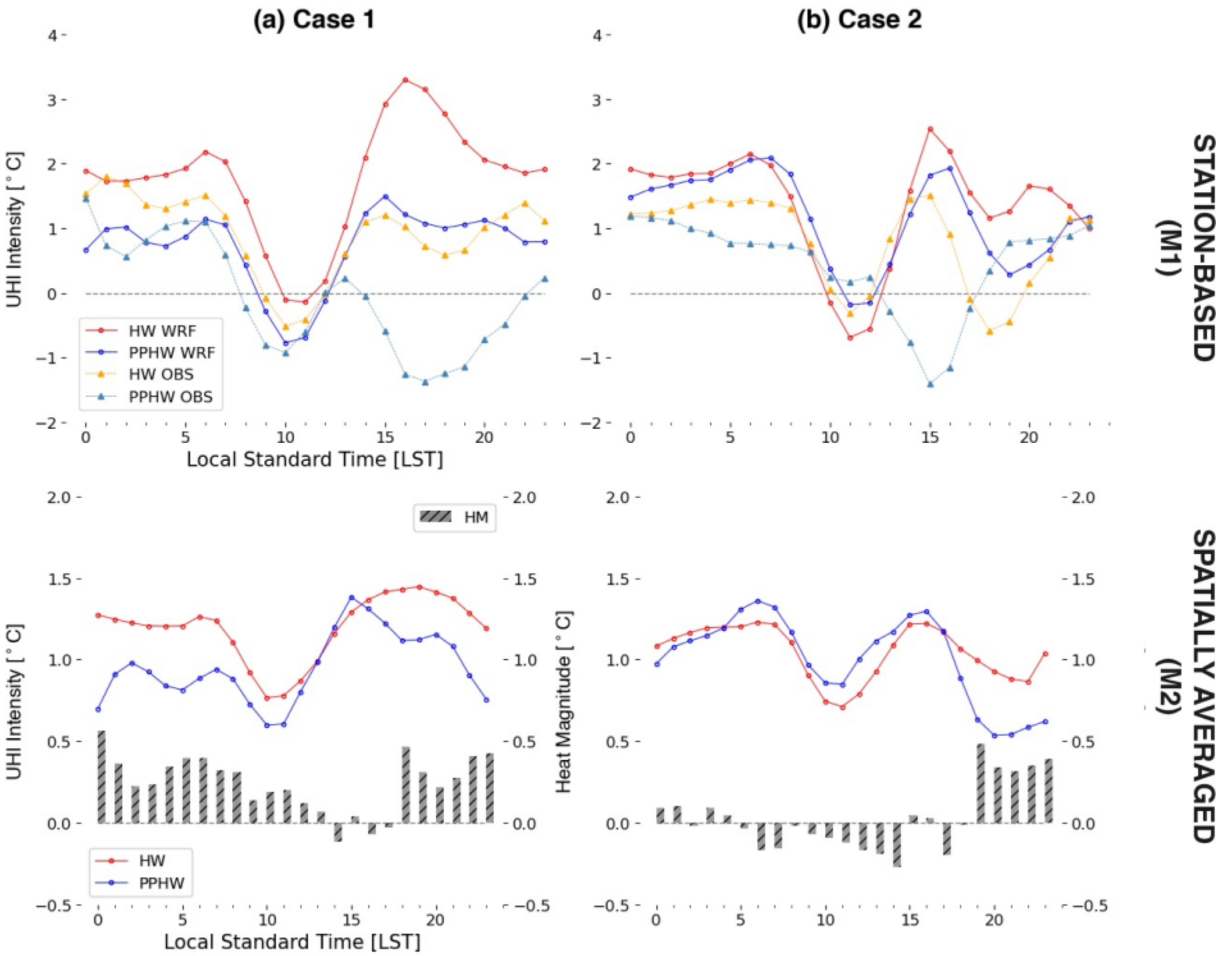

FIGURE 7 UHII pattern and heat magnitude/heat load (HM) changes. The top panel displays the comparison of station-based (M1) UHII profiles between model simulation and observation stations. The bottom panel displays the spatially averaged (M2) diurnal UHII profiles from the simulation (URB–non-URB), denoted by the solid line, while the bar plot indicates the HM changes, calculated from the difference of UHII during HW to PPHW days. Values above 0 indicate additional HM, and below 0 indicate reduced HM. M1 computation involves data from four urban stations, PJ, SER, SBG and KLIA, and two rural stations, JA and SBL. M2 values for each category are calculated by spatially averaging the T2 of all grids (within d03), as discussed in section 2.6. [Colour figure can be viewed at wileyonlinelibrary.com]

and simulate the patterns and intensity of solar radiation, which are essential for driving the thermal and dynamic processes within the model. As shown in Figure 6, the model data closely matched the observed data, demonstrating intense goodness of fit. Specifically, the coefficient of determination (R^2) was notably high, reaching approximately 0.93 (HW in Case 1), 0.90 (HW in Case 2), 0.73 (PPHW in Case 1) and 0.80 (PPHW in Case 2). In other words, the model performance was superior during HW conditions compared to PPHW conditions, aligning with other bias assessments conducted for T2 and RH.

3.3 | UHI–HW interaction

The interaction between UHI and HW is a complex phenomenon involving intricate relationships between urban environments and extreme heat events. This section discusses the diurnal variations and spatial patterns of the UHII in response to HW and PPHW days. UHII analysis is conducted using the "station-based" (M1) and spatially averaged method (averaging values from multiple grid points within each category) under distinct URB and non-URB settings (M2), as outlined in section 2.6. The utilisation of both the M1 and M2 settings in our study serves different purposes and provides complementary insights into the UHI dynamics and their interaction with HW events. M1 enables localized UHI examination. Conversely, M2 provides a broader perspective, averaging values across URB and non-URB categories, facilitating a larger-scale assessment and spatial UHII distribution analysis across the entire study area. Besides the computational methodology distinction between M1 and M2, the M2 method also largely eliminates the impact of sea breezes, clouds and topography on surface temperature (Bohnenstengel et al., 2011; Li et al., 2013). Both methods are essential for a thorough knowledge of UHI–HW dynamics. The daytime analysis in this study spans from 0700 to 1900 LST, with the remaining period covering night-time. All the analyses and results presented herein are based on the averaged term.

The WRF-UCM replicated the temporal trend of the UHI profiles in both cases, as illustrated in Figure 7. During the daytime, it is typical to observe a minimal temperature difference between urban and rural areas owing to the abundance of incoming solar radiation, accelerating the heating process over both surfaces. The lower heating rate experienced in urban areas compared to rural environments during the daytime results in a subdued UHI difference, especially within the initial 4 h after sunrise, and is known as the urban cool island (UCI) (Theeuwes et al., 2015). This cooling phase lasted for 3–5 h, followed by a notably swift temperature increase propelled by the higher sensible heat flux in urban areas, as shown in the same figure. This temperature surge was most prominent during the late afternoon and extended to night-time. Notably, the cooler daytime temperature pattern was not evident in simulation M2, indicating that the non-URB settings consistently produced lower temperatures, resulting in a positive UHII.

From the same figure, a notable increase in the UHII during the HW was detected in both the actual measurements and simulations. UHII increments were observed with additional heat loads measured in all scenarios, except for the daytime UHII in simulation M2 for Case 2, which exhibits a slightly reduced heat load of −0.06°C. This minimal reduction can be attributed to the slightly lower temperatures produced by the URB setting and the relatively higher temperatures produced by the non-URB setting for type 12 (croplands) during HW. According to Harun et al. (2020), the shading effect of high-rise buildings in Kuala Lumpur contributes to reducing UHII and can create a cool island effect during the day. Conversely, croplands tend to be warmer and absorb more heat (Wickham et al., 2012) because they are less obstructed by downward solar radiation. These conditions may have minimised the differences between URB and non-URB settings, potentially leading to an underestimation of the daytime UHII peak. Consequently, the average daytime heat load for this specific case slightly decreased. The results of the UHII and heat load analyses are presented in Table 6. Clearly, the degree of the UHII was most pronounced during the night-time and heightened during HW. However, the maximum peak was observed during the daytime. It is also evident that simulation M2 consistently provides lower UHII values than the direct measurements, which is attributed to spatial averaging that smooths local variations and reduces the impact of extremes. Figure 8 illustrates a discernible contrast in the spatial distribution of the nocturnal UHII during the HW and PPHW periods.

3.4 | Heat fluxes responses to HW

Quantifying the energy components within surface energy balance models is essential for understanding the energy exchange during HW and PPHW days, particularly in urban areas. The observation of global solar radiation data clearly highlights a substantial increase during HW conditions compared to PPHW conditions in both cases (see Figure 4). In Case 1, the peak occurred at 1400 LST, registering 1083.3 $W{\cdot}m^{-2}$ during HW and 750.0 $W{\cdot}m^{-2}$ during PPHW. Similarly, in Case 2, higher global solar radiation was recorded with a peak of 888.9 $W{\cdot}m^{-2}$ compared to the PPHW, with 805.6 $W{\cdot}m^{-2}$ at 1300 LST. This finding aligns with observations of cloud cover at urban stations.

An examination of the ground heat flux, Q_G as depicted in Figure 9, provides valuable insights into the distinction in heat storage between urban and rural areas. Notably, Q_G simulations in urban environments exhibit a substantial increase during HW owing to the heightened heat storage within the urban infrastructure, including pavements, buildings and other structures. Consequently, this elevation in Q_G contributes to amplified night-time urban temperatures during HW days in comparison to PPHW days, with nocturnal heat loads reaching 0.8°C in Case 1 and 0.4°C in Case 2 (see Figure 8).

Figure 10 shows the cumulative sensible heat flux Q_H simulated using the WRF model. The use of the cumulative Q_H allowed us to capture the cumulative effect of heat transfer over time, providing valuable insights into the overall heat dynamics during HW events. The intensification of Q_H during HW was evident in both urban and rural areas, indicating the influence of extreme heat events on heat dynamics. Furthermore, the contrasting patterns between urban and rural regions during these events emphasise the role of variations in urbanisation factors. In Case 1, the daytime average cumulative Q_H from the ground surface of the urban area exhibited a growth rate of 0–2361.1 $W{\cdot}m^{-2}$ during HW days, indicating increased heat transfer from the urban surface to the atmosphere. This growth rate surpassed that of PPHW days by 289.7 $W{\cdot}m^{-2}$, indicating a higher magnitude of heat flux during HW events. In Case 2, with a growth rate of 0–2083.3 $W{\cdot}m^{-2}$ during the HW period and PPHW days exceeding 135.0 $W{\cdot}m^{-2}$. A similar anomaly is

TABLE 6 UHII and heat magnitude/heat load (HM) analysis.

		UHII								HM			
		HW				PPHW							
		Day		Night		Day		Night		Day		Night	
Case	Method	Average	Peak	Average	Peak	Average	Peak	Average	Peak	Average	Max	Average	Max
1	Observation	0.5°C	1.5°C (0700 LST)	1.4°C	1.8°C (0100 LST)	−0.5°C	0.9°C (0700 LST)	0.5°C	1.5°C (0000 LST)	1.0°C	2.3°C (1600 LST)	0.9°C	1.8°C (2100 LST)
	Simulation M1	1.7°C	3.3°C (1600 LST)	1.9°C	2.1°C (2000 LST)	0.6°C	1.5°C (1600 LST)	0.9°C	1.1°C (0600 LST)	1.1°C	2.3°C (1800 LST)	1.0°C	1.2°C (0000 LST)
	Simulation M2	1.1°C	1.5°C (1900 LST)	1.3°C	1.4°C (2000 LST)	0.9°C	1.5°C (1600 LST)	0.9°C	1.2°C (2000 LST)	0.2°C	0.5°C (1800 LST)	0.4°C	0.6°C (0000 LST)
2	Observation	0.6°C	1.7°C (1500 LST)	1.1°C	1.5°C (0600 LST)	0.0°C	0.9°C (0800 LST)	1.0°C	1.2°C (0100 LST)	0.6°C	3.7°C (1500 LST)	0.1°C	0.7°C (0600 LST)
	Simulation M1	1.1°C	2.6°C (1600 LST)	1.7°C	2.0°C (0500 LST)	1.0°C	2.2°C (0700 LST)	1.4°C	1.9°C (0600 LST)	0.1°C	1.5°C (1900 LST)	0.3°C	1.1°C (2100 LST)
	Simulation M2	1.0°C	1.3°C (1600 LST)	1.1°C	1.2°C (0300 LST)	1.1°C	1.4°C (1700 LST)	0.9°C	1.3°C (0600 LST)	−0.1°C	0.5°C (1900 LST)	0.2°C	0.4°C (2300 LST)

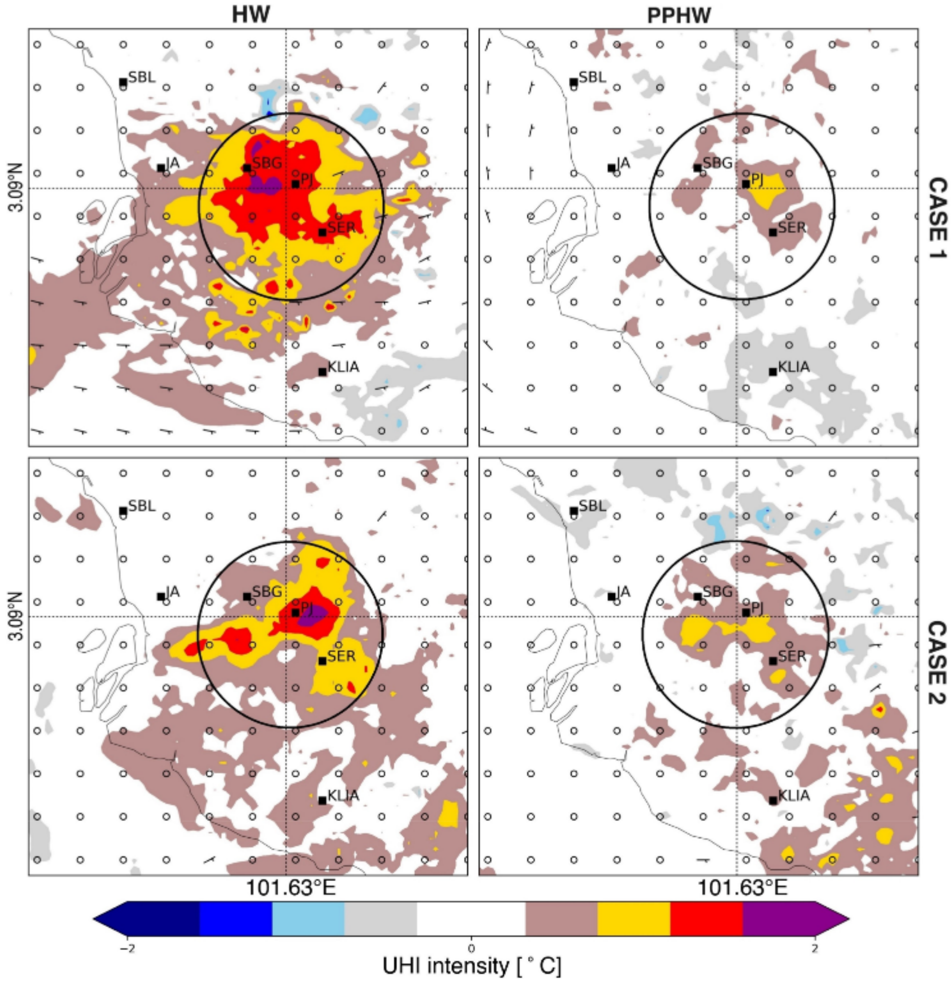

FIGURE 8 The spatial distribution of nocturnal UHII in the GKL area during HW days on April 3, 2016 (Case 1) and April 19, 2020 (Case 2). The peaks reached 1.9 and 1.8°C in Cases 1 and 2, respectively. The same information for PPHW days, April 6, 2016 (Case 1) and April 17, 2020 (Case 2), had peaks at 1.1 and 1.4°C in Cases 1 and 2, respectively. The black circle serves as a marker, indicating the centre of the urban area. [Colour figure can be viewed at wileyonlinelibrary.com]

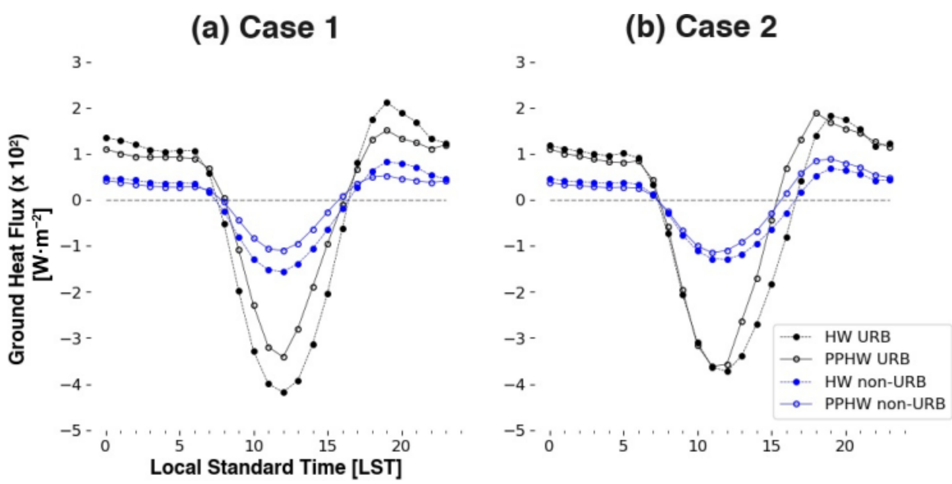

FIGURE 9 The ground heat flux, Q_G profiles during HW on April 3, 2016 (Case 1) and April 19, 2020 (Case 2) and, PPHW April 6, 2016 (Case 1) and April 17, 2020 (Case 2). Two distinct categories are distinguished by colour: black for URB and blue for non-URB. The average values are calculated by spatially averaging the Q_G of all grids (within d03) for each category. [Colour figure can be viewed at wileyonlinelibrary.com]

observed in rural areas, with an average cumulative Q_H difference of 498.5 W·m^{-2} for Case 1 and 286.9 W·m^{-2} for Case 2 when comparing HW to PPHW days. Here, the term "rural" refers to the results obtained using the M2 method, which provides a broader-scale analysis for a comprehensive assessment of UHI dynamics across the entire study area.

Additionally, the analysis of Bowen's ratio values underscores a notable difference between urban and rural areas, with these differences becoming more pronounced during the HW. In urban environments, Bowen Ratio values in hourly averages exceed 20 in Case 1 and 8 in Case 2, indicating the prevalence of Q_H, whereas in rural areas, Bowen Ratio values remain below 2 in both

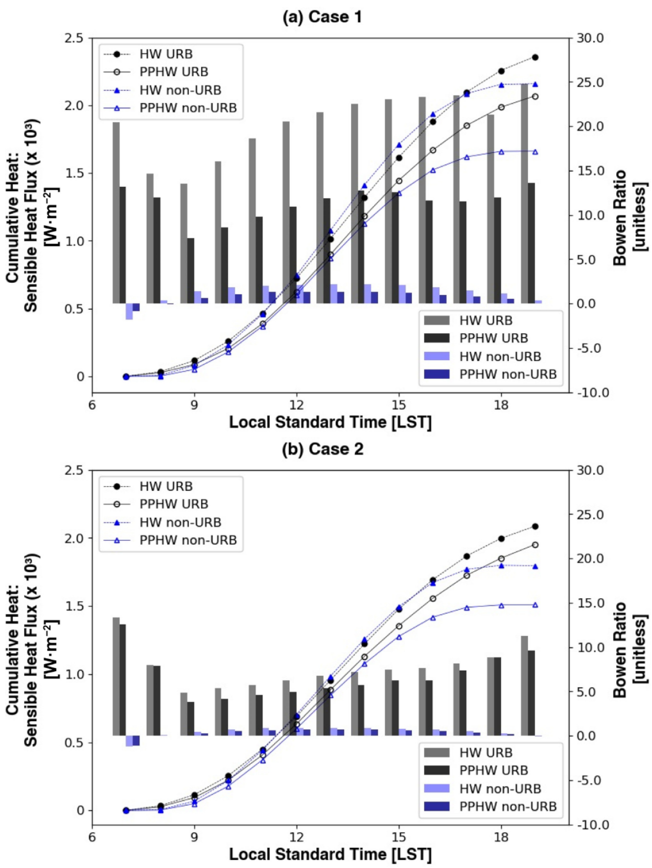

FIGURE 10 Spatially averaged cumulative Q_H and Bowen Ratio measurements during daytime for HW and PPHW days, with (a) corresponds to Case 1 analysis, while (b) for Case 2. The line plots represent cumulative Q_H, while the bar plots depict Bowen Ratio. Two distinct categories are distinguished by colour: black for URB and blue for non-URB. The average values are calculated by spatially averaging the Q_H of all grids (within d03) for each category. The persistence of a higher Bowen Ratio during HW episodes indicates intensified heat transfer mechanisms, primarily driven by Q_H, in urban areas. [Colour figure can be viewed at wileyonlinelibrary.com]

cases, highlighting the dominance of latent heat flux, Q_E. The widening gap in Bowen Ratio values between urban and rural areas during HW events reflects the distinct heat dynamics in these environments.

4 | DISCUSSION

From the results discussed in the previous section, urbanisation clearly induced surface temperatures in the GKL and amplified the UHI effect. In the context of the GKL and urban warming, our study underscores the prevailing dominance of the nocturnal UHII over its daytime counterpart, which is consistent with prior numerical studies (Morris et al., 2016a, 2016b; Ooi et al., 2017). During HW, amplification of UHII heightened and increased the heat magnitude or heat loads during daytime/night-time by 1.0°C/0.9°C (observation), 1.1°C/1.0°C (simulation M1) and 0.2°C/0.4°C (simulation M2) in Case 1 and 0.6°C/0.1°C (observation), 0.1°C/0.3°C (simulation M1) and −0.1°C/0.2°C (simulation M2) in Case 2. UHII amplification was more prominent in Case 1 than in Case 2. Despite both cases occurring in record-warm years, a notable difference existed in their ENSO conditions. Case 1 occurring within a stronger El Niño year, which resulted in an abundance of solar radiation reaching the Earth's surface due to reduced cloudiness during the episodes. In contrast, Case 2 occurred during an early 2020 neutral year. During HW, the maximum UHII peak is likely to occur at noon, consistent with a study in Shanghai (Ao et al., 2019) with observed heat loads reached 2.3°C at 1600 LST in Case 1 and 3.7°C at 1500 LST in Case 2. The daytime UHII peak correlated with the surplus solar radiation received under HW conditions (see Figure 4). For instance, the global solar radiation peak during HW surpasses the PPHW days by 304.6 W·m^{-2} in Case 1 and exceeds by 83.3 W·m^{-2} in Case 2. This condition significantly boosts daytime Q_H owing to sparse vegetation coverage and the absence of surface moisture in urban areas (Ao et al., 2019; Meng et al., 2011).

Regarding the surface energy budget, there is a pronounced change in Q_H, Q_E, Q_G and net radiation during the HW in the GKL. Compared with normal days, the ground absorbs a substantial amount of heat input during HW and increases heat storage, particularly in urban areas with heat-absorbing surfaces such as asphalt and concrete. At night, ground heat loss prolongs Q_H release elevates night-time temperatures and is amplified during HW. This is evident with elevated of average nocturnal UHII during HW at 1.4, 1.9 and 1.3°C in Case 1, and 1.1, 1.7 and 1.1°C in Case 2, for observation, and simulations M1 and M2, respectively. Our results are consistent with those of most studies in the literature that show a positive UHI–HW synergy.

As no other NWP studies have examined UHI–HW synergy in the GKL area, our findings are juxtaposed with those of Chew et al. (2020) for Singapore, a tropical coastal city in SEA. Their study corresponds to Case 1 of our research, conducted during the same HW year in April. In contrast to our findings, their conclusion asserted no observed UHII amplification during HW, with heat storage fluxes remaining unchanged compared to normal days. Although the GKL and Singapore are part of the maritime continent, their unique geographical contexts may contribute to differences in the UHI–HW interactions. GKL's proximity to the coast allows pronounced land–sea breeze interactions (Ooi et al., 2017).

In contrast, Singapore, an island city at the southern tip of Peninsular Malaysia, is surrounded by smaller islands and relatively narrow water bodies, which may result in different land–sea breeze dynamics. These geographical differences can affect local microclimates, including temperature distribution, wind patterns and humidity levels, which, in turn, influence the UHI effects and heatwave interactions observed between the two cities.

In addition, solar radiation distribution differed significantly between the two cases. During the HW in GKL, there was a marked increase in solar radiation compared to PPHW days, which was not observed in Singapore. This increase in solar radiation during the HW in the GKL likely contributed to the higher surface temperatures and a more pronounced UHII. Although there was a discrepancy in the observed UHI–HW synergy between GKL and Singapore, neither case demonstrated significant changes in wind speed during the HW. According to Ao et al. (2019), the diverse outcomes of the UHI–HW synergy across cities stem from various physical mechanisms, including heightened increases in urban net radiation and AHE input under HW conditions. The study also revealed that UHII amplification was more pronounced when the regional wind speed was reduced and under the influence of sea breezes during HW. Hence, the careful selection of reference stations, particularly in areas close to the coast, significantly affected the UHII amplification results under the influence of HW.

Furthermore, a comparison of the findings across different climates provided additional insights. For instance, studies in temperate cities, such as Shanghai (Ao et al., 2019) and Seoul (Ngarambe et al., 2020), showed that maximum UHII peaks occurred at different times of the day and exhibited varied heat load intensities during HW events. In Shanghai, the synergistic effect was most pronounced at noon, whereas in Seoul, it occurred between noon and late at night. In contrast, Zhao et al. (2018) discovered that daytime synergy effects in cities with dry climates are negligible in the current climate but develop in the future. These differences underscore the complexity of UHI–HW interactions, which are influenced by urban morphology, local climatic conditions and regional atmospheric dynamics. Understanding these variations is crucial for developing effective mitigation strategies tailored to specific urban environments.

Notably, the tropics exhibit unique features compared to temperate climates, such as differences in atmospheric circulation patterns, moisture availability and land–sea interactions. In tropical regions, higher humidity levels during heat waves can exacerbate heat stress owing to the reduced effectiveness of evaporative cooling, which is less of a concern in temperate climates, where humidity levels are generally lower. Additionally, diurnal temperature variations are typically smaller in tropical regions, making the impact of heat waves potentially more severe owing to sustained high temperatures throughout the day and night. Furthermore, in areas with distinct seasons, such as temperate zones, heat waves may occur during specific periods of the year, often coinciding with the summer peak (e.g., Hua et al., 2023; Robine et al., 2007; Russo et al., 2015). In contrast, tropical regions may experience heat waves at any time of the year because seasonal temperature variations are less pronounced. This lack of seasonality can contribute to the unpredictability and frequency of heat waves in tropical areas, posing continuous challenges to adaptation and mitigation.

We highlight some limitations that could potentially influence the study outcomes. First, the utilisation of spatially distributed AHE data, which is essential for capturing localised heat sources and their impact on UHI intensity. However, the existing data do not explicitly consider extreme events such as heat waves. The AHE data adopted from Varquez et al. (2021) are based on data from the International Institute of Applied Systems Analysis (IIASA) and the 2010 records of country-level gross domestic product (GDP) from The World Bank. This data source may have affected the accuracy of the simulation results, particularly for 2020, considering the 10-year time difference. Using more accurate and up-to-date information regarding the spatial distribution of anthropogenic heat during the study period could have led to more pronounced differences in heat loads. The AHE input is expected to be higher during HW, leading to a stronger synergistic influence in the future. Future research should consider obtaining more detailed AHE data, including information on energy consumption during heat waves compared to normal days, to improve the precision of the study's findings.

Second, consider integrating urban morphological characteristics into the WRF model to gain more realistic heterogeneities in the city. While it is essential to acknowledge the advancements offered by newer land use data frameworks, such as the Local Climate Zone (LCZ) classification, and platforms such as WUDAPT (Chen & Hu, 2022; Ren et al., 2016), our current analysis using the MODIS dataset remains robust and credible, especially when simulating extreme heat events. Despite its age, the MODIS dataset is highly regarded for its reliability in land cover classification, vegetation mapping and climate modelling at regional and global scales (Ganguly et al., 2010; Gaur et al., 2020; Jin et al., 2005; Mallick et al., 2020; Nandini et al., 2022; Wickham et al., 2012). In urban climate research for GKL, the dataset is frequently used as a standard reference for land cover and vegetation information (e.g., Hamray &

Choi, 2022; Li et al., 2020; Morris et al., 2016a, 2016b), making it reliable for the current study. With the recent advancements in WRF version 4.6, including the availability of explicit distributions of urban parameters, future studies stand to benefit significantly from leveraging these new features. In future work, we aim to improve the spatial resolution and fidelity of our simulations to better capture the heterogeneous nature of urban areas. Specifically, we plan to explore the utilisation of LCZ classification and incorporate detailed urban morphological parameters into the WRF, enhancing the accuracy and reliability of our modelling outcomes.

Third, this study is limited by the analysis of only two extreme HW events occurring in the most recent years. Both cases coincided with specific ENSO conditions known to influence the strength and magnitude of HW (Li et al., 2020), which showed an amplification of UHII in GKL. However, it is important to recognize that the findings may not be fully generalizable. The limited number of cases means that different or additional HW events might produce varying results. Future studies should consider a broader range of HW cases, including those occurring in different seasons and under varying climatic conditions, to validate the findings and provide a more comprehensive understanding of the UHI–HW interaction.

5 | CONCLUSION AND REMARKS

This study, employing the WRF-UCM, represents the most recent numerical study investigating the synergistic interaction between UHI and HW in GKL, a tropical urban area in Malaysia. We examined the 2 m temperature behaviour and surface energy budget variations during HW and PPHW days. This study focused on specific cases of extreme HW events that occurred in 2016 and 2020, which are recognised as among the top three warmest years on record. The selection of these cases was based on the computation of the HWMId. The conclusions of this study are as follows.

1. A heightened UHII is evident during heat waves in both observations and simulations, particularly pronounced during night-time with average heat loads of 0.9°C (observation), 1.0°C (simulation M1) and 0.4°C (simulation M2) in Case 1, and 0.1°C (observation), 0.3°C (simulation M1) and 0.2°C (simulation M2) in Case 2.
2. During heat waves, both observations and simulations exhibited a UHII peak during the daytime, consistent with the surplus solar radiation manifested during the day compared to PPHW days. The observed maximum heat loads are likely to occur at noon with a magnitude increase of 2.3°C at 1600 LST in Case 1 and 3.7°C at 1500 LST in Case 2.
3. Analysis of the heat flux components from the surface energy balance model provided empirical support for the synergy between the UHI and HW.
   a. The recorded global radiation data at the urban station showed an increase in radiation during the HW compared to the PPHW conditions for both cases. The most pronounced variation in hourly averages was recorded at 1500 LST, with 433.0 W·m^{-2} in Case 1, and at 1600 LST, with 243.1 W·m^{-2} in Case 2.
   b. A significant increase in cumulative daytime Q_H was observed during HW days compared to PPHW days in both urban and rural areas. The average cumulative Q_H difference is notable, reaching 289.7 W·m^{-2} in Case 1, and 135.0 W·m^{-2} in Case 2 for urban and 498.5 W·m^{-2} in Case 1 and 286.9 W·m^{-2} in Case 2, for rural.
   c. The Bowen Ratio consistently increased during the transition from the HW to PPHW conditions. The most prominent increase was observed, reaching 11.9 at 1700 LST in Case 1 and 1.4 at 1600 LST in Case 2 for urban areas. There is a remarkable contrast in the Bowen Ratio between urban and rural areas, with hourly averages exceeding 20 in Case 1 and 8 in Case 2 in urban settings, while remaining below 2 in both cases in rural environments.

This study can potentially provide invaluable insights, particularly in urban planning. The ongoing urbanisation trends in Malaysia accentuate the relevance of these insights. In 2020, Malaysia achieved a notable urbanisation rate of 79%, which is expected to increase further to approximately 85% by 2040, as outlined in the Third National Physical Plan (NPP-3) (PLANMalaysia, 2022). In the face of rapid urbanisation, a deep understanding of the intricate dynamics of UHI and their interplay with extreme weather events, such as heat waves, has become increasingly crucial. Leveraging the capabilities of numerical predictions in urban climate modelling can play a significant role in addressing the challenges posed by global warming.

Furthermore, the findings provide essential guidance for urban planners and policymakers by influencing critical urban development, infrastructure and climate resilience decisions. This study has the potential to significantly contribute to Kuala Lumpur's vision, as articulated in the Kuala Lumpur Climate Action Plan 2050 (KLCAP2050). Incorporating the insights derived from this research can empower stakeholders to tackle the challenges associated with urban heat and heat waves more effectively, ultimately enhancing the well-being and comfort of urban residents in swiftly urbanising Malaysia. In addition, comparing the two cases, it appears that the occurrence of heat waves under specific ENSO conditions may influence the strength and magnitude of the UHII in cities. Research on this topic could aid future planning and mitigation strategies for urban residents vulnerable to extreme weather events. Given the distinctive nature of each case, further research is imperative to establish a consensus on this relationship, particularly in vulnerable tropical urban regions.

AUTHOR CONTRIBUTIONS

Sharifah Faridah Syed Mahbar: Conceptualization; methodology; software; data curation; investigation; validation; formal analysis; visualization; writing – original draft. **Hiroyuki Kusaka:** Conceptualization; methodology; supervision; funding acquisition; project administration; resources; writing – original draft.

ACKNOWLEDGEMENTS

This research was supported by JSPS KAKENHI Grant Number JP24K07130. This research was partly supported by Multidisciplinary Cooperative Research Program in Center for Computational Sciences, University of Tsukuba. We thank the Malaysian Meteorological Department (MET Malaysia) for providing the observational data used in our statistical analysis and verifying and validating our model simulations. We also thank our group member, Nobuyasu Suzuki, for his technical support in the WRF-UCM modification. The first author would like to express her gratitude to the Public Service Department of Malaysia for the scholarships.

CONFLICT OF INTEREST STATEMENT

The authors declare no conflicts of interest.

DATA AVAILABILITY STATEMENT

The data that support the findings of this study are available from the corresponding author upon reasonable request. Some of the data are subject to the provisions outlined in the Data Act, which preclude their sharing.

ORCID

Hiroyuki Kusaka https://orcid.org/0000-0002-0326-7179

REFERENCES

Ahmad Kamal, N.I., Ash'aari, Z.H. & Abdullah, A.M. (2019) Spatio-temporal variability of heat exposure in Peninsular Malaysia using land surface temperature. *Disaster Advances*, 12(12), 1–9.

Ao, X., Wang, L., Zhi, X., Gu, W., Yang, H. & Li, D. (2019) Observed synergies between urban heat islands and heat waves and their controlling factors in Shanghai, China. *Journal of Applied Meteorology and Climatology*, 55, 1955–1972. Available from: https://doi.org/10.1175/JAMC-D-19-0073.1

Arifwidodo, S.D. & Chandrasiri, O. (2020) Urban heat stress and human health in Bangkok, Thailand. *Environmental Research*, 185, 109398. Available from: https://doi.org/10.1016/j.envres.2020.109398

Bohnenstengel, S.I., Evans, S., Clark, P.A. & Belcher, S.E. (2011) Simulations of the London urban heat island. *Quarterly Journal of the Royal Meteorological Society*, 137, 1625–1640. Available from: https://doi.org/10.1002/qj.855

Chen, F., Kusaka, H., Bornstein, R., Ching, J., Grimmond, C.S.B., Grossman-Clarke, S. et al. (2011) The integrated WRF/urban modeling system: development, evaluation, and applications to urban environmental problems. *International Journal of Climatology*, 31, 273–288. Available from: https://doi.org/10.1002/joc.2158

Chen, Y. & Hu, Y. (2022) The urban morphology classification under local climate zone scheme based on the improved method—a case study of Changsha, China. *Urban Climate*, 45, 101271. Available from: https://doi.org/10.1016/j.uclim.2022.101271

Chew, L.W., Liu, X., Li, X.X. & Norford, L.K. (2020) Interaction between heat wave and urban heat island: a case study in a tropical coastal city, Singapore. *Atmospheric Research*, 247, 105134. Available from: https://doi.org/10.1016/j.atmosres.2020.105134

Department of Statistics Malaysia. (2018) Newsletter. DOSM/BPPIB/1.2018/Series 10. Available from: www.dosm.gov.my [Accessed on 6th June 2023]

Dimiceli, V.E., Piltz, S.F. & Amburn, S.A. (2012) Black Globe Temperature Estimate for the WBGT Index. *IAENG Transactions on Engineering Technologies*, (pp. 323–334). Available from: https://doi.org/10.1007/978-94-007-4786-9_26

Doan, Q.-V. & Kusaka, H. (2016) Numerical study on regional climate change due to the rapid urbanization of greater Ho Chi Minh City's metropolitan area over the past 20 years. *International Journal of Climatology*, 36, 3633–3650. Available from: https://doi.org/10.1002/joc.4582

Doan, Q.-V., Kusaka, H. & Ho, Q.-B. (2016) Impact of future urbanization on temperature and thermal comfort index in a developing tropical city: Ho Chi Minh City. *Urban Climate*, 17, 20–31. Available from: https://doi.org/10.1016/j.uclim.2016.04.003

Dong, Z., Wang, L., Sun, Y., Hu, T., Limsakul, A., Singhruck, P. et al. (2021) Heatwaves in Southeast Asia and their changes in warmer world. *Earth's Futures*, 9, e2021EF001992. Available from: https://doi.org/10.1029/2021EF001992

Dudhia, J. (1989) Numerical study of convection observed during the winter monsoon experiment using a mesoscale two-dimensional model. *Journal of the Atmospheric Sciences*, 46, 3077–3107. Available from: https://doi.org/10.1175/1520-0469(1989)046<3077:NSOCOD>2.0.CO;2

Elsayed, I.S.M. (2012) Mitigation of the urban heat island of the city of Kuala Lumpur, Malaysia. *Middle-East Journal of Scientific Research*, 11(11), 1602–1613. Available from: https://doi.org/10.5829/9dosi.mejsr.2012.11.11.1590

Ganguly, S., Friedl, M.A., Tan, B., Zhang, X. & Verma, M. (2010) Land surface phenology from MODIS: Characterization of the collection 5 global land cover dynamics product. *Remote Sensing of Environment*, 114, 1805–1816. Available from: https://doi.org/10.1016/j.rse.2010.04.005

Gaur, A., Lacasse, M., Armstrong, M., Lu, H., Shu, C., Fields, A. et al. (2020) Effects of using different urban parametrization schemes and land-cover datasets on the accuracy of WRF model over City of Ottawa. *Urban Climate*, 35, 100737. Available from: https://doi.org/10.1016/j.uclim.2020.100737

Golzio, A., Ferrarese, S., Cassardo, C., Diolaiuti, G.A. & Pelfini, M. (2021) Land-use improvements in the weather research and forecasting model over complex mountainous terrain and comparison of different grid sizes. *Boundary-layer Meteorology*, 180, 319–351. Available from: https://doi.org/10.1007/s10546-021-00617-1

Hamray, N.S.M. & Choi, M. (2022) Effects of heat waves on urban warming across different urban morphologies and climate zones. *Building and Environment*, 209(2022), 108677. Available from: https://doi.org/10.1016/j.buildenv.2021.108677

Harun, Z., Reda, E., Abdulrazzaq, A., Abbas, A.A., Yusup, Y. & Zaki, S.A. (2020) Urban heat island in the modern tropical Kuala Lumpur: comparative weight of the different parameters. *Alexandria Engineering Journal*, 59, 4475–4489. Available from: https://doi.org/10.1016/j.aej.2020.07.053

Hong, S., Noh, Y. & Dudhia, J. (2006) A new vertical diffusion package with an explicit treatment of entrainment processes. *Monthly Weather Reviews*, 134, 2318–2341. Available from: https://doi.org/10.1175/MWR3199.1

Hua, W., Dai, A., Qin, M., Hu, Y. & Cui, Y. (2023) How unexpected was the 2022 summertime heat extremes in the middle reaches of the Yangtze River. *Geophysical Research Letters*, 50, E2023GL104269. Available from: https://doi.org/10.1029/2023GL104269

Huang, B., Liu, C., Banzon, V., Freeman, E., Graham, G., Hankins, B. et al. (2021) Improvements of daily optimum interpolation sea surface temperature (DOISST) version 2.1. *Journal of Climate*, 34(8), 2923–2939. Available from: https://doi.org/10.1175/JCLI-D-20-0166.1

Husin, M.Z., Usman, I.M.S. & Suratman, R. (2021) Density challenges of high-rise residential development in Malaysia. *Journal of the Malaysian Institute of Planners*, 19(4), 96–109.

Imran, H.M., Hossain, A., Islam, A.K.M.S., Rahman, A., Bhuiyan, M.A.E., Paul, S. et al. (2021) Impact of land cover changes on land surface temperature and human thermal comfort in Dhaka City of Bangladesh. *Earth Systems and Environment*, 5, 667–693. Available from: https://doi.org/10.1007/s41748-021-00243-4

Isa, N.A., Salleh, S.A., Wan Mohd, W.M.N., Ooi, M.C.G., Chan, A. & Islam, M.A. (2020) Impacts of lateral boundary condition resolution in tropical urban climate modelling for Kuala Lumpur. *Engineering Journal*, 25(1), 165–175.

Jaiswal, R.K., Lohani, A.K. & Tiwari, H.L. (2015) Statistical analysis for change detection and trend assessment in climatological parameters. *Environmental Processes*, 2, 729–749. Available from: https://doi.org/10.1007/s40710-015-0105-3

Jamaluddin, A.F., Tangang, F., Cung, J.X., Juneng, L., Sasaki, H. & Takayabu, I. (2018) Investigating the mechanism of diurnal rainfall variability over Peninsular Malaysia using the non-hydrostatic regional climate model. *Meteorology and Atmospheric Physics*, 130, 611–633. Available from: https://doi.org/10.1007/s00703-017-0541-x

Jiang, S., Lee, X., Wang, J. & Wang, K. (2019) Amplified urban heat islands during heat wave periods. *Journal of Geophysical Research: Atmospheres*, 124, 7797–7812. Available from: https://doi.org/10.1029/2018JD030230

Jin, M., Dickinson, R.E. & Zhang, D.-L. (2005) The footprint of Urban Areas on Global Climate as characterized by MODIS. *Journal of Climate*, 18(10), 1551–1565. Available from: https://doi.org/10.1175/JCLI3334.1

Klysik, K. & Fortuniak, K. (1999) Temporal and spatial characteristics of urban heat island of Lodz, Poland. *Atmospheric Environment*, 33, 3885–3895.

Kondo, H. & Kikegawa, Y. (2003) Temperature variation in the Urban Canopy with anthropogenic energy use. *Pure and Applied Geophysics*, 160, 317–324.

Kumar, R. & Mishra, V. (2019) Decline in surface urban heat island intensity in India during heatwaves. *Environmental Research Communications*, 1, 031001. Available from: https://doi.org/10.1088/2515-7620/ab121d

Kusaka, H., Chen, F., Tewari, M., Dudhia, J., Gill, D.O., Duda, M.G. et al. (2012b) Numerical simulations of urban heat island effect by the WRF model with 4-km grid increment: an inter-comparison study between urban canopy model and slab model. *Journal of the Meteorological Society of Japan*, 90B, 33–45.

Kusaka, H., Hara, M. & Takane, Y. (2012a) Urban climate projection by the WRF Model at 3-km horizontal grid increment: dynamical downscaling and predicting heat stress in the 2070's August for Tokyo, Osaka, and Nagoya Metropolises. *Journal of the Meteorological Society of Japan*, 90B, 47–63. Available from: https://doi.org/10.2151/jmsj.2012-B04

Kusaka, H. & Kimura, F. (2004) Coupling a single-layer urban canopy model with a simple atmospheric model: impact on urban heat island simulation for an idealized case. *Journal of the Meteorological Society of Japan*, 82(1), 67–80.

Kusaka, H., Kondo, H. & Kikegawa, Y. (2001) A simple single-layer urban canopy model for atmospheric models: comparison with multi-layer and slab models. *Boundary-Layer Meteorology*, 101, 329–358. Available from: https://doi.org/10.1023/A:1019207923078

Li, D. & Bou-Zeid, E. (2013) Synergistic interactions between urban heat islands and heat waves: the impact in cities is larger than the sum of its parts. *Journal of Applied Meteorology and Climatology*, 52, 2051–2064. Available from: https://doi.org/10.1175/JAMC-D-13-02.1

Li, D., Sun, T., Liu, M., Wang, L. & Gao, Z. (2016) Changes in wind speed under heat waves enhance urban heat islands in the Beijing Metropolitan Area. *American Meteorological Society*, 55, 2369–2375. Available from: https://doi.org/10.1175/JAMC-D-16-0102.1

Li, X.-X. (2020) Heat wave trends in Southeast Asia during 1979–2018: the impact of humidity. *Science of the Total Environment*, 721, 137664. Available from: https://doi.org/10.1016/j.scitotenv.2020.137664

Li, X.-X., Koh, T.-Y., Entekhabi, D., Roth, M., Panda, J. & Norford, L.K. (2013) A multi-resolution ensemble study of a tropical urban environment and its interactions with the background regional atmosphere. *Journal of Geophysical Research:*

Atmospheres, 118, 9804–9818. Available from: https://doi.org/10.1002/jgrd.50795

Li, Y., Fowler, H.J., Argüeso, D., Blenkinsop, S., Evans, J.P., Lenderink, G. et al. (2020) Strong intensification of hourly rainfall extremes by urbanization. *Geophysical Research Letters*, 47, e2020GL088758. Available from: https://doi.org/10.1029/2020GL088758

Magnaye, A.M.T. & Kusaka, H. (2024) Potential effect of urbanization on extreme heat events in Metro Manila Philippines using WRF-UCM. *Sustainable Cities and Society*, 110, 105584. Available from: https://doi.org/10.1016/j.scs.2024.105584

Mallick, J., Hang, T.H., Rahman, A., Hasan, M.A., Ibrahim, F. & Ahmed, M. (2020) Assessing inter-seasonal variations of vegetation cover and land surface temperature in the NCR using MODIS data. *Applied Ecology and Environmental Research*, 18(3), 4241–4258. Available from: https://doi.org/10.15666/aeer/1803_42414258

Meng, W.-G., Zhang, Y.-X., Li, J.-N., Lin, W.-S., Dai, G.-F. & Li, H.-R. (2011) Application of WRF/UCM in the simulation of a heat wave event and urban heat island around Guangzhou. *Journal of Tropical Meteorology*, 17(3), 257–267.

Mlawer, E.J., Taubman, S.J., Brown, P.D., Iacono, M.J. & Clough, S.A. (1997) Radiative transfer for inhomogeneous atmospheres: RRTM, a validated correlated–k model for the longwave. *Journal of Geophysical Research*, 102, 16663–16682. Available from: https://doi.org/10.1029/97JD00237

Mohd Rasfan. (2016) Severe heatwave grips Malaysia. Available from: https://www.aljazeera.com/news/2016/4/11/severe-heatwave-grips-malaysia [Accessed on 17th November 2022]

Morris, K.I., Chan, A., Salleh, S.A., Ooi, M.C.G., Oozeer, M.Y. & Abakr, Y.A. (2016a) Numerical study on the urbanisation of Putrajaya and its interaction with the local climate, over a decade. *Urban Climate*, 16, 1–24. Available from: https://doi.org/10.1016/j.uclim.2016.02.001

Morris, K.I., Chan, A., Morris, K.J.K., Ooi, M.C.G., Oozeer, M.Y., Abakr, Y.A. et al. (2016b) Urbanisation and urban climate of a tropical conurbation, Klang Valley, Malaysia. *Urban Climate*, 19, 54–71. Available from: https://doi.org/10.1016/j.uclim.2016.12.002

Nandini, G., Vinoj, V., Sethi, S.S., Nayak, H.P., Landu, K., Swain, D. et al. (2022) A modelling study on quantifying the impact of urbanization and regional effects on the wintertime surface temperature over a rapidly-growing tropical city. *Computational Urban Science*, 2, 40. Available from: https://doi.org/10.1007/s43762-022-00067-6

Ngarambe, J., Nganyiyimana, J., Kin, I., Santamouris, M. & Yun, G.Y. (2020) Synergies between urban heat island and heat waves in Seoul: the role of wind speed and land use characteristics. *PLoS One*, 15(12), e0243571. Available from: https://doi.org/10.1371/journal.pone.0243571

Niu, G., Yang, Z.-L., Mitchell, K.E., Chen, F., Ek, M.B., Barlage, M. et al. (2011) The community Noah land surface model with multiparameterization options (Noah–MP): 1. Model description and evaluation with local-scale measurements. *Journal of Geophysical Research*, 116, D12109. Available from: https://doi.org/10.1029/2010JD015139

Oke, T.R. (1973) City size and the urban heat island. *Atmospheric Environment*, 7, 769–779.

Ooi, M.C.G., Chan, A., Ashfold, M.J., Morris, K.I., Oozer, M.Y. & Salleh, S.A. (2017) Numerical study on effect of urban heating on local climate during calm inter-monsoon period in Greater Kuala Lumpur, Malaysia. *Urban Climate*, 20, 228–250. Available from: https://doi.org/10.1016/j.uclim.2-17.04.010

Ooi, M.C.G., Chan, A., Ashfold, M.J., Oozer, M.Y., Morris, K.I. & Kong, S.S.K. (2018b) The role of land use in the local climate and air quality during calm inter-monsoon in a tropical city. *Geoscience Frontiers*, 10, 405–415. Available from: https://doi.org/10.1016/j.gsf.2018.04.005

Ooi, M.C.G., Chan, A., Kumarenthiran, S., Morris, K.I., Oozeer, M.Y., Islam, M.A. et al. (2018a) Comparison of WRF local and nonlocal boundary layer physics in Greater Kuala Lumpur, Malaysia. *IOP Conference Series: Earth and Environmental Science*, 117, 012015.

PLANMalaysia. (2022) https://myplan.planmalaysia.gov.my/www/admin/uploads_publication/rancangan-fizikal-negara-ke-3-chapter-1-en-06012022.pdf [Accessed on 1st August 2023]

Puley, G., Calhoun, A.G. & Toruteva, L. (2022) Extreme heat preparing for the heatwaves of the future. A joint publication of the United Nations Office for the Coordination of Humanitarian Affairs, the International Federation of Red Cross and Red Crescent Societies, and the Red Cross Red Crescent Climate Centre. Available from: https://www.ifrc.org/sites/default/files/2022-10/Extreme-Heat-Report-IFRC-OCHA-2022.pdf

Ramakreshnan, L., Aghamohammadi, N., Fong, C.S., Ghaffarianhoseini, A., Wong, L.P. & Sulaiman, N.M. (2018) Empirical study on temporal variations of canopy-level urban heat island effect in the tropical city of Greater Kuala Lumpur. *Sustainable Cities and Society*, 44, 748–762. Available from: https://doi.org/10.1016/j.scs.2018.10.039

Ramamurthy, P. & Bou-Zeid, E. (2016) Heatwaves and urban heat islands: a comparative analysis of multiple cities. *Journal of Geophysical Research: Atmospheres*, 122, 168–178. Available from: https://doi.org/10.1002/2016JD025357

Ren, C., Cai, M., Wang, R., Xu, Y. & Ng, E. (2016) *Local climate zone (LCZ) classification using World Urban Database and Access Portal Tools (WUDAPT) method: a case study in Wuhan and Hangzhou.* Paper presented at the forth international conference on countermeasure to urban heat islands (4th IC2UHI), May 30–31 to June 1, 2016, Stephen Riady Centre, University Town, NUS. Available from: https://www.reserachgate.net/publication/303754082

Robine, J.-M., Cheung, S.L.K., le Roy, S., van Oyen, H., Griffiths, C., Michel, J.P. et al. (2007) Death toll exceeded 70,000 in Europe during summer of 2003. *Comptes Rendus Biologies*, 331, 171–178. Available from: https://doi.org/10.1016/j.crvi.2007.12.001

Russo, S., Dosio, A., Graversen, R.G., Sillmann, J., Carrao, H., Dunbar, M.B. et al. (2014) Magnitude of extreme heat waves in present climate and their projection in a warming world. *Journal of Geophysical Research: Atmospheres*, 119, 12500–12512. Available from: https://doi.org/10.1002/2014JD022098

Russo, S., Sillmann, J. & Fisher, E.M. (2015) Top ten European heatwaves since 1950 and their occurrence in the coming decades. *Environmental Research Letters*, 10, 124003.

Sailor, D.J. (2010) A review of methods for estimating anthropogenic heat and moisture emissions in the urban environment. *International Journal of Climatology*, 31, 189–199. Available from: https://doi.org/10.1002/joc.2106

Scott, A.A., Waugh, D.W. & Zaitchik, B.F. (2018) Reduced urban heat island intensity under warmer condition. *Environmental Research Letters*, 13, 064004. Available from: https://doi.org/10.1088/1748-9326/aabd6c

Shaharuddin, A., Noorazuan, M.H., Takeuchi, W. & Noraziah, A. (2014) The effects of urban heat islands on human comfort: a case of Klang Valley Malaysia. *Global Journal on Advances in Pure & Applied Sciences*, 2, 1–8.

Sham, S. (1972) Some aspects of urban microclimate of Kuala Lumpur, West Malaysia. *Akademika*, 1, 85–92.

Sham, S. (1990) Urban climatology in Malaysia: an overview. *Energy and Buildings*, 15(16), 105–117.

Stafoggia, M., Forastiere, F., Agostini, D., Caranci, N., de'Donato, F., Demaria, M. et al. (2008) Factors affecting in-hospital heat-related mortality: a multi-city case-crossover analysis. *Journal of Epidemiology and Community Health*, 62, 209–215. Available from: https://doi.org/10.1136/jech.2007.060715

Tangang, L., Farzanmanesh, R., Mirzaei, S.A., Salimun, E., Jamaluddin, A.F. & Juneng, L. (2017) Characteristics of precipitation extremes in Malaysia associated with El Niño and La Niña events. *International Journal of Climatology*, 37, 696–716. Available from: https://doi.org/10.1002/joc.5032

Tapiador, F.J., Navarro, A., Levizzani, V., García-Ortega, E., Huffman, G.J., Kidd, C. et al. (2017) Global precipitation measurements for validating climate models. *Atmospheric Research*, 197, 1–20. Available from: https://doi.org/10.1016/j.atmosres.2017.06.021

Tewari, M., Yang, J., Kusaka, H., Salamanca, F., Watson, C. & Treinish, L. (2019) Interaction of urban heat islands and heat waves under current and future climate conditions and their mitigation using green and cool roofs in New York and Phoenix, Arizona. *Environmental Research Letters*, 14, 034002. Available from: https://doi.org/10.1088/1748-9326/aaf431

The Star/Asia News Network. (2016) More falling ill in Malaysia as heatwave takes its toll. Available from: https://www.straitstimes.com/asia/se-asia/more-falling-ill-in-malaysia-as-heatwave-takes-its-toll [Accessed on 17th November 2022]

Theeuwes, N.E., Steeneveld, G.-J., Ronda, R.J., Rotach, M.W. & Holtslag, A.A.M. (2015) Cool city mornings by urban heat. *Environmental Research Letters*, 10, 114022.

Thirumalai, K., DiNezio, P.N., Okumura, Y. & Deser, C. (2017) Extreme temperatures in Southeast Asia caused by El Niño and worsened by global warming. *Nature Communications*, 8, 15531. Available from: https://doi.org/10.1038/ncomms15521

Thompson, G., Field, P.R., Rasmussen, R.M. & Hall, W.D. (2008) Explicit forecasts of winter precipitation using an improved bulk microphysics scheme. Part II: implementation of a new snow parameterization. *Monthly Weather Reviews*, 136, 5095–5115. Available from: https://doi.org/10.1175/2008MWR2387.1

Varquez, A.C.G., Kiyomoyo, S., Khanh, D.N. & Kanda, M. (2021) Global 1-km present and future hourly anthropogenic heat flux. *Science Data*, 8, 64. Available from: https://doi.org/10.1038/s41597-021-00850-w

Varquez, A.C.G., Nakayoshi, M., Makabe, T. & Kanda, M. (2014) WRF application of high resolution urban surface parameters on some major cities of Japan. *Journal of Japan Society of Civil Engineering*, 70(4), 175–180. Available from: https://doi.org/10.2208/jscejhe.70.1_175

Vitanova, L.L. & Kusaka, H. (2018) Study on the urban heat island in Sofia City: Numerical simulations with potential natural vegetation and present land use data. *Sustainable Cities and Society*, 40, 110–125. Available from: https://doi.org/10.1016/j.scs.2018.03.012

Vitanova, L.L., Kusaka, H., Doan, Q.-V. & Subasinghe, S. (2021) How urban growth changes the heat island effect and human thermal sensations over the last 100 years and towards the future in European city? *Meteorological Applications*, 28, e2019. Available from: https://doi.org/10.1002/met.2019

Wang, J.-W., Yang, H.-J. & Kim, J.-J. (2020) Wind speed estimation in urban areas based on the relationships between background wind speeds and morphological parameters. *Journal of Wind Engineering & Industrial Aerodynamics*, 205, 104324. Available from: https://doi.org/10.1016/j.jweia.2020.104324

Wang, W. et al. (2019) Weather research & forecasting model: ARW version 4 modelling system user's guide. Available from: http://www2.mmm.ucar.edu/wrf/users/ [Accessed on 8th August 2022]

Ward, K., Lauf, S., Kleinschmit, B., & Endlicher, W. (2016) Heat waves and urban heat islands in Europe: a review of relevant drivers. *Science of the Total Environment*, 527–539. http://dx.doi.org/10.1016/j.scitotenv.2016.06.119

Wickham, J.D., Wade, T.G. & Riitters, K.H. (2012) Comparison of cropland and forest surface temperatures across the conterminous United States. *Agricultural and Forest Meteorology*, 166–167, 137–143. Available from: https://doi.org/10.1016/j.agrformet.2012.07.002

Yang, Z., Niu, G.-Y., Mitchell, K.E., Chen, F., Ek, M.B., Barlage, M. et al. (2011) The community Noah land surface model with multiparameterization options (Noah–MP): 2. Evaluation over global river basins. *Journal of Geophysical Research*, 116, D12110. Available from: https://doi.org/10.1029/2010JD015140

Yasin, M.Y., Mohd Zain, M.A. & Hassan, M.H. (2022) Urbanization and growth of Greater Kuala Lumpur: issues and recommendations for urban growth management. *Southeast Asia*, 22(2), 4–19.

Zhang, C. & Wang, Y. (2017) Projected future changes of tropical cyclone activity over the Western North and South Pacific in a 20-km-Mesh Regional Climate Model. *Journal of Climate*, 30, 5923–5941. Available from: https://doi.org/10.1175/JCLI-D-16-0597.1

Zhao, L., Oppenheimer, M., Zhu, Q., Baldwin, J.W., Ebi, K.L., Bou-Zeid, E. et al. (2018) Interactions between urban heat islands and heat waves. *Environmental Research Letters*, 13, 034003. Available from: https://doi.org/10.1088/1748-9326/aa9f73

SUPPORTING INFORMATION

Additional supporting information can be found online in the Supporting Information section at the end of this article.

How to cite this article: Syed Mahbar, S. F., & Kusaka, H. (2024). Synergistic interactions between urban heat islands and heat waves in the Greater Kuala Lumpur and surrounding areas. *International Journal of Climatology*, *44*(13), 4886–4906. https://doi.org/10.1002/joc.8614